# Electronic Structure and Spectro-Structural Correlations of Fe(III)Zn(II) Biomimetics for Purple Acid Phosphatases: Relevance to DNA Cleavage and Cytotoxic Activity

Rosely A. Peralta,[†] Adailton J. Bortoluzzi,[†] Bernardo de Souza,[†] Rafael Jovito,[†] Fernando R. Xavier,[†] Ricardo A. A. Couto,[†] Annelise Casellato,[†] Faruk Nome,[†] Andrew Dick,[‡] Lawrence. R. Gahan,[‡] Gerhard Schenk,[‡] Graeme R. Hanson,[§] Flávia C. S. de Paula,[||] Elene C. Pereira-Maia,[||] Sergio de P. Machado,[⊥] Patricia C. Severino,[#] Claus Pich,[#] Tiago Bortolotto,[#] Hernán Terenzi,[#] Eduardo E. Castellano,[▽] Ademir Neves,*,[†] and Mark J. Riley*,[‡]

[†]*Departamento de Química, Universidade Federal de Santa Catarina, Florianópolis, South Carolina 88040-900, Brazil,* [‡]*School of Chemistry and Molecular Biosciences, The University of Queensland, St. Lucia, QLD 4072, Australia,* [§]*Centre for Advanced Imaging, The University of Queensland, St. Lucia, QLD 4072, Australia,* [||]*Departamento de Química, Universidade Federal de Minas Gerais, Belo Horizonte, MG, 31270-901, Brazil,* [⊥]*Departamento de Química Inorgânica, Instituto de Química, Universidade Federal do Rio de Janeiro, Rio de Janeiro, RJ, 21941-909, Brazil,* [#]*Departamento de Bioquímica, Universidade Federal de Santa Catarina, Florianópolis, South Carolina 88040-900, Brazil, and* [▽]*Instituto de Física de São Carlos, Departamento de Física e Informática, Universidade de São Paulo, São Carlos, SP, 13566-590, Brazil*

Purple acid phosphatases (PAPs) are a group of metallohydrolases that contain a dinuclear Fe(III)M(II) center (M(II) = Fe, Mn, Zn) in the active site and are able to catalyze the hydrolysis of a variety of phosphoric acid esters. The dinuclear complex $[(H_2O)Fe^{III}(\mu\text{-}OH)Zn^{II}(\textbf{L-H})](ClO_4)_2$ (**2**) with the ligand 2-[*N*-bis(2-pyridylmethyl)aminomethyl]-4-methyl-6-[*N'*-(2-pyridylmethyl)(2-hydroxybenzyl) aminomethyl]phenol (H₂**L-H**) has recently been prepared and is found to closely mimic the coordination environment of the Fe(III)Zn(II) active site found in red kidney bean PAP (Neves et al. *J. Am. Chem. Soc.* **2007**, *129*, 7486). The biomimetic shows significant catalytic activity in hydrolytic reactions. By using a variety of structural, spectroscopic, and computational techniques the electronic structure of the Fe(III) center of this biomimetic complex was determined. In the solid state the electronic ground state reflects the rhombically distorted Fe(III)N₂O₄ octahedron with a dominant tetragonal compression aligned along the $\mu$-OH−Fe−O$_{phenolate}$ direction. To probe the role of the Fe−O$_{phenolate}$ bond, the phenolate moiety was modified to contain electron-donating or -withdrawing groups (−CH₃, −H, −Br, −NO₂) in the 5-position. The effects of the substituents on the electronic properties of the biomimetic complexes were studied with a range of experimental and computational techniques. This study establishes benchmarks against accurate crystallographic structural information using spectroscopic techniques that are not restricted to single crystals. Kinetic studies on the hydrolysis reaction revealed that the phosphodiesterase activity increases in the order −NO₂ ← Br ← H ← CH₃ when 2,4-bis(dinitrophenyl)phosphate (2,4-bdnpp) was used as substrate, and a linear free energy relationship is found when $\log(k_{cat}/k_0)$ is plotted against the Hammett parameter $\sigma$. However, nuclease activity measurements in the cleavage of double stranded DNA showed that the complexes containing the electron-withdrawing −NO₂ and electron-donating −CH₃ groups are the most active while the cytotoxic activity of the biomimetics on leukemia and lung tumoral cells is highest for complexes with electron-donating groups.

## Introduction

Purple acid phosphatases (PAPs) are a group of metallo-hydrolases that contain a heterovalent dinuclear Fe(III)M(II) center (M(II) = Fe, Mn, Zn) in the active site, and which are able to catalyze the hydrolysis of a variety of phosphoric acid esters and anhydrides within the pH range 3−8.[1−4] In the structure of red kidney bean PAP (rkbPAP)[1,4,5] the Fe(III) ion is coordinated to a tyrosine (Y167), a histidine (H325) and an aspartate (D135) while the Zn(II) ion is coordinated by two

*To whom correspondence should be addressed. E-mail: ademir@qmc.ufsc.br (A.N.), m.riley@uq.edu.au (M.J.R.).

(1) Klabunde, T.; Sträter, N.; Fröhlich, R.; Witzel, H.; Krebs, B. *J. Mol. Biol.* **1996**, *259*, 737–748.

(2) Mitić, N.; Smith, S. J.; Neves, A.; Guddat, L. W.; Gahan, L. R.; Schenk, G. *Chem. Rev.* **2006**, *106*, 3338–3363.

(3) Mitić, N.; Valizadeh, M.; Leung, E. W. W.; de Jersey, J.; Hamilton, S.; Hume, D. A.; Cassady, A. I.; Schenk, G. *Arch. Biochem. Biophys.* **2005**, *439*, 154–164.

(4) Schenk, G.; Elliott, T. W.; Leung, E. W. W.; Mitić, N.; Carrington, L. E.; Gahan, L. R.; Guddat, L. W. *BMC Struct. Biol.* **2008**, *8*, 6.

(5) Truong, N. T.; Naseri, J. I.; Vogel, A.; Rompel, A.; Krebs, B. *Arch. Biochem. Biophys.* **2005**, *440*, 38–45.
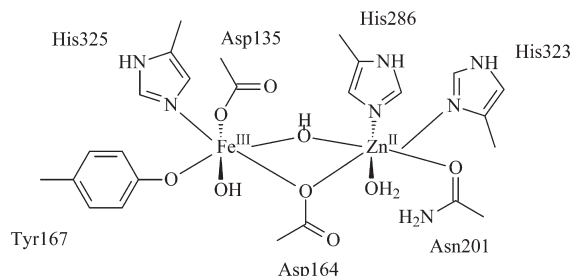
**Figure 1.** Representative active site of purple acid phosphatases (PAPs). The residue labels refer to red kidney bean PAP (rkbPAP).

histidines (H286, H323) and an asparagine (N201). The $Fe^{III}Zn^{II}$ center is bridged by a monodentate carboxylate group of an aspartate (D164) and by a $\mu$-hydroxo group. While crystallographically ambiguous, terminal hydroxo and aqua ligands were also modeled to complete the 6-fold coordination spheres of the $Fe^{III}$ and $Zn^{II}$ ions, respectively, resulting in the $[(OH)Fe^{III}(\mu\text{-}OH)Zn^{II}(OH_2)]$ core[1] as shown in Figure 1.

Because of the relatively low resolution of protein crystal structures, in particular related to PAPs enzymes,[1,2,4] model complexes often play an important role in the structural characterization of the active sites in metalloproteins. Recently, we have established a general method for the preparation of mixed-valence heterobinuclear $Fe^{III}M^{II}$ complexes using the unsymmetrical donor ligand 2-[N-bis-(2-pyridylmethyl)-aminomethyl]-4-methyl-6-[N'-(2-pyridylmethyl)(2-hydroxybenzyl) aminomethyl]phenol ($H_2$**L-H**). The unsymmetric ligand **L-H**$^{2-}$ has both hard ($N_2O_2$) and soft ($N_3O$) sites that bind the $Fe^{III}$ and $M^{II}$ ions, respectively, with vacant coordinating sites available for bridging ligands. The complexes $Fe^{III}Fe^{II}$**L-H**, $Fe^{III}Zn^{II}$**L-H**, $Fe^{III}Mn^{II}$**L-H**, $Fe^{III}Ni^{II}$**L-H**, $Fe^{III}Cu^{II}$**L-H**, $Fe^{III}$-$Co^{II}$**L-H**, and $Ga^{III}Zn^{II}$**L-H** containing two bidentate acetate bridging ions have previously been reported.[6−13] These complexes contain a terminal $Fe^{III}$-phenolate motif that results in the characteristic purple color of the chromophore because of an intense ligand to metal charge transfer (LMCT) transition in the visible region of the spectrum. In the solid state most of these complexes have two acetate bridges, in contrast to the enzymes where a (hydr)oxide links the two metal ions.[1−4]

**Chart 1.** General Structure of Complexes **1−4** (R = $CH_3$, H, Br, $NO_2$)
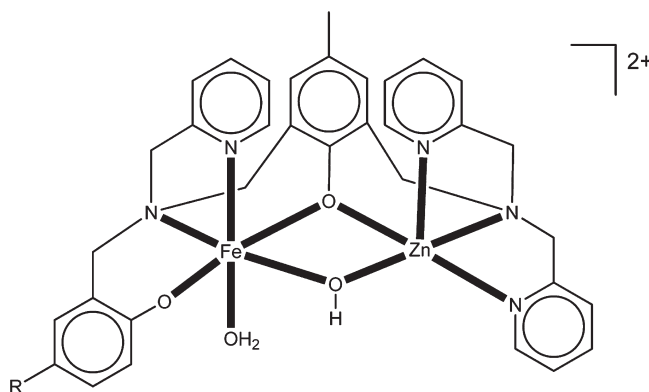


However, under suitable conditions it has been possible to prepare the $[H_2OFe^{III}(\mu\text{-}OH)Zn^{II}$**L-H**$]^{2+}$ complexes without the bridging acetates.[14] In these complexes the bridging acetates are replaced by a $\mu$-$OH^-$ bridge and a terminally bound water to the $Fe^{III}$, with the $M^{II}$ ion becoming five coordinate. Their structures can be described as a distorted octahedron edge sharing with a distorted trigonal bipyramid.

Metalloproteins with tyrosine bound to iron, such as lactoferrin[15] and PAPs,[2,15−17] show intense colors because of the tyrosinate-to-iron(III) LMCT bands.[17,18] Their enzymatic activity is considered to be related to the $Fe^{III}/Fe^{II}$ potential,[19] which will also affect the energy of these LMCT bands. It has been demonstrated in a series of high-spin Schiff base iron(III) complexes that these LMCT bands shift to higher energies, and that the $Fe^{III}/Fe^{II}$ redox potential becomes more negative as the number of phenolate-containing donor sites increases.[20] These relationships have been pursued using a series of monomeric iron complexes with two phenolate ligands,[21] and where the electronic properties of the phenolate group itself is varied by substitutions in the position *para* to the phenolate oxygen.

Herein we report the geometric and electronic structure and the phosphodiesterase-like activity of the $[H_2OFe^{III}$-$(\mu\text{-}OH)Zn^{II}$**L-R**$]^{2+}$ (R = $-CH_3$, $-H$, $-Br$, $-NO_2$) series of complexes (**1−4**) in detail (Chart 1). Since $Zn^{II}$ is spectroscopically silent, this series of complexes enables the study of the $S = 5/2$ high spin $Fe^{III}$ center in the catalytic site and the LMCT spectra associated with the $Fe^{III}$-phenolate chromophore, without magnetic coupling effects in the ground state. Specifically, structural (X-ray crystallography) and spectroscopic (electron paramagnetic resonance (EPR), magnetic circular dichroism (MCD), and UV−vis) techniques, as well as electrochemical, potentiometric titration, and kinetic

(6) Batista, S. C.; Neves, A.; Bortoluzzi, A. J.; Vencato, I.; Peralta, R. A.; Szpoganicz, B.; Aires, V. V. E.; Terenzi, H.; Severino, P. C. *Inorg. Chem. Commun.* **2003**, *6*, 1161–1165.

(7) Karsten, P.; Neves, A.; Bortoluzzi, A. J.; Lanznaster, M.; Drago, V. *Inorg. Chem.* **2002**, *41*, 4624–4625.

(8) Lanznaster, M.; Neves, A.; Bortoluzzi, A. J.; Aires, V. V. E.; Szpoganicz, B.; Terenzi, H.; Severino, P. C.; Fuller, J. M.; Drew, S. C.; Gahan, L. R.; Hanson, G. R.; Riley, M. J.; Schenk, G. *J. Biol. Inorg. Chem.* **2005**, *10*, 319–332.

(9) Lanznaster, M.; Neves, A.; Bortoluzzi, A. J.; Szpoganicz, B.; Schwingel, E. *Inorg. Chem.* **2002**, *41*, 5641–5643.

(10) Neves, A.; de Brito, M.; Vencato, I.; Drago, V.; Griesar, K.; Haase, W. *Inorg. Chem.* **1996**, *35*, 2360–2368.

(11) Schenk, G.; Peralta, R. A.; Batista, S. C.; Bortoluzzi, A. J.; Szpoganicz, B.; Dick, A.; Herrald, P.; Hanson, G. R.; Szilagyi, R. K.; Riley, M. J.; Gahan, L. R.; Neves, A. *J. Biol. Inorg. Chem.* **2008**, *13*, 139–155.

(12) Smith, S. J.; Casellato, A.; Hadler, K. S.; Mitić, N.; Riley, M. J.; Bortoluzzi, A. J.; Szpoganicz, B.; Schenk, G.; Neves, A.; Gahan, L. R. *J. Biol. Inorg. Chem.* **2007**, *12*, 1207–1220.

(13) Xavier, F. R.; Neves, A.; Casellato, A.; Peralta, R. A.; Bortoluzzi, A. J.; Szpoganicz, B.; Severino, P. C.; Terenzi, H.; Tomkowicz, Z.; Ostrovsky, S.; Haase, W.; Ozarowski, A.; Krzystek, J.; Telser, J.; Schenk, G.; Gahan, L. R. *Inorg. Chem.* **2009**, *48*, 7905–7921.

(14) Neves, A.; Lanznaster, M.; Bortoluzzi, A. J.; Peralta, R. A.; Casellato, A.; Castellano, E. E.; Herrald, P.; Riley, M. J.; Schenk, G. *J. Am. Chem. Soc.* **2007**, *129*, 7486–7487.

(15) Anderson, B. F.; Baker, H. M.; Dodson, E. J.; Norris, G. E.; Rumball, S. V.; Waters, J. M.; Baker, E. N. *Proc. Natl. Acad. Sci. U.S.A.* **1987**, *84*, 1769–1773.

(16) Averill, B. A.; Davis, J. C.; Burman, S.; Zirino, T.; Sanders-Loehr, J.; Loehr, T. M.; Sage, J. T.; Debrunner, P. G. *J. Am. Chem. Soc.* **1987**, *109*, 3760–3767.

(17) Yang, Y. S.; McCormick, J. M.; Solomon, E. I. *J. Am. Chem. Soc.* **1997**, *119*, 11832–11842.

(18) Ainscough, E. W.; Brodie, A. M.; Plowman, J. E.; Brown, K. L.; Addison, A. W.; Gainsford, A. R. *Inorg. Chem.* **1980**, *19*, 3655–3663.

(19) Bradley, F. C.; Lindstedt, S.; Lipscomb, J. D.; Que, L., Jr.; Roe, A. L.; Rundgren, M. *J. Biol. Chem.* **1986**, *261*, 11693–11696.

(20) Ramesh, K.; Mukherjee, R. *J. Chem. Soc., Dalton Trans.* **1992**, *1*, 83–89.

(21) Lanznaster, M.; Neves, A.; Bortoluzzi, A. J.; Assumpção, A. M. C.; Vencato, I.; Machado, S. P.; Drechsel, S. M. *Inorg. Chem.* **2006**, *45*, 1005–1011.

measurements, are used to show (i) how the structural and electronic properties of the series of $[H_2OFe^{III}(\mu\text{-}OH)Zn^{II}\text{-}L\text{-}R]^{2+}$ complexes are affected by the substituent R on the phenolate ring, (ii) how these properties change upon dissolving the solid complexes, (iii) how the hydrolase-like activity (using a model substrate and DNA) and the cytotoxic activity (IC50) of **1−4** are affected by the electron donor/acceptor nature of the substituent on the terminally bound phenolate. Importantly, it is demonstrated for complexes **1−4** that after monodentate binding of the substrate to the $Zn^{II}$ center, the terminal $Fe^{III}$-bound hydroxide rather than the bridging hydroxide acts as the initiating nucleophile in the hydrolysis of a diester phosphate. Such a mechanism is in agreement with that proposed for the monoesterase activity of rkbPAP,[22−25] thus demonstrating that the model system does not only mimic the two chemically distinct geometric environments around the $Fe^{III}$ and $Zn^{II}$ centers in the enzyme, but also shares functional similarities.[1,14]

## Experimental Section

**Materials and Methods.** All starting materials were purchased from Aldrich, Acros, or Merck. ^{1}H NMR spectra were recorded with a Bruker-FT 200 MHz instrument at room temperature, and the chemical shifts referenced to the residual solvent ($CDCl_3$) signal. IR spectra were recorded with a Perkin-Elmer-FTIR 2000 spectrophotometer (KBr pellet). Tetrabutylammonium hexafluorophosphate ($TBAPF_6$) was recrystallized from ethanol, 2-pyridinecarboxyaldehyde was distilled under reduced pressure, and 2,4-dinitrophenol was recrystallized from chloroform. The substrate bis-(2,4-dinitrophenyl)phosphate (2,4-bdnpp) was synthesized, characterized, and purified as described in the literature.[26] Elemental analyses were made in a CHNS analyzer from Carlo Erba model E-1110. Electronic spectra were recorded with a Perkin-Elmer Lambda-19 spectrometer in quartz cuvettes of 1 cm path-length. All electrochemical experiments (recorded in a potentiostat-galvanostat PAR 273) requiring an inert atmosphere were performed in a conventional three-electrode cell filled with ultrapure argon. Data were collected using a typical three-electrode electrochemical cell. The auxiliary electrode was a platinum sheet. The reference electrode consisted of $Ag/Ag^+$, and the working electrode was a glassy carbon previously polished in an alumina slurry to a 0.3 $\mu m$ finish. $TBAPF_6$ or NaCl was used as the supporting electrolyte. The redox pair $Fc^+/Fc$ (or sodium hexacyanoferrate) was used as an internal standard.[27]

**Preparation of Ligands.** A general synthetic route for the preparation of the ligands H₂**L**-R (R = −CH₃, −H, −Br, −NO₂) is shown in Scheme S1 in the Supporting Information. The ligands 2-[*N*-bis-(2-pyridylmethyl)aminomethyl]-4-methyl-6-[*N′*-(2-pyridylmethyl)(2-hydroxybenzyl)aminomethyl]phenol (H₂**L-H**),[7] and 2-[*N*-bis-(2-pyridylmethyl)aminomethyl]-4-methyl-6-[*N′*-(2-pyridylmethyl)(2-hydroxy-5-nitrobenzyl)aminomethyl]phenol (H₂**L-NO₂**)[28] were synthesized as previously reported.

**2-[*N*-bis-(2-pyridylmethyl)aminomethyl]-4-methyl-6-[*N′*-(2-pyridylmethyl)(2-hydroxy-5-methylbenzyl)aminomethyl]phenol; H₂L-CH₃.** The ligand *N*-(2-hydroxy-5-methylbenzyl)(2-pyridylmethyl)amine (hbpa-CH₃) was obtained as follows: 2.7 g (20 mmol) of 2-(aminomethyl)pyridine was added to a methanolic solution containing 2.2 g (20 mmol) of 2-hydroxy-5-methylbenzaldehyde under stirring. After 1 h, 0.76 g (20 mmol) of sodium borohydride was slowly added. The pH was then adjusted to 6.0 using 2.0 mol $L^{-1}$ HCl, and the solvent evaporated under reduced pressure. A 100 mL portion of $CH_2Cl_2$ was added to the remaining solid, the solution was washed with a sodium bicarbonate saturated aqueous solution ($5 \times 40$ mL), dried over anhydrous sodium sulfate, and the solvent removed under vacuum. A 3.4 g portion (15 mmol) of hbpa-CH₃ was obtained as a pale yellow oil. Yield 75%. IR (KBr) in $cm^{-1}$: $\nu$(N−H) 3445; $\nu$(C−H$_{ar}$ and C−H$_{aliph}$) 3013−2918; $\nu$(C=N and C=C) 1594−1435; $\nu$(C−O) 1253; $\nu$(C−N) 1148; $\nu$(C−H$_{ar}$) 769. ^{1}H NMR, $\delta_H$ (200 MHz; CDCl₃), in ppm: 2.15 (s, 3H); 3.84 (s, 2H); 3.87 (s, 2H); 5.97 (s, 1 H, NH); 6.64−6.70 (m, 3H); 6.87−6.94 (dt, 1H); 7.14−7.17 (dd, 1H); 7.56−7.64 (dt, 1H); 8.49−8.52 (d, 1H).

The ligand H₂**L-CH₃** was synthesized by adding to a 60 mL of $CH_2Cl_2$ solution containing 8.77 g of 2-[*N*-bis(2-pyridylmethyl)-aminomethyl]-4-methyl-6-chloromethylphenol hydrochloride - bpmamcf·HCl[7] (21.7 mmol), 4.95 g of hbpa-CH₃ (21.7 mmol), and 3.5 g of triethylamine (25 mmol) previously dissolved in 50 mL of $CH_2Cl_2$. After reflux for 36 h, the mixture was washed with an aqueous sodium bicarbonate solution ($5 \times 40$ mL), dried over anhydrous $Na_2SO_4$, and the solvent removed under vacuum. The yellow solid remaining was dissolved in acetone and after some hours under refrigeration the pale yellow solid obtained was collected by filtration, washed with cold acetone, and dried in air. Yield: 10.6 g, 90%; mp 86−88 °C; IR (KBr) cm$^{-1}$: $\nu$(C−H$_{Ar}$ and C−H$_{aliph}$) 3055−2824; $\nu$(C=C) 1594−1434; $\nu$(O−H) 1372; $\nu$(C−O$_{phenol}$) 1252−1229; $\nu$(C−H$_{Ar}$) 757. ^{1}H NMR (200 MHz; CDCl₃): $\delta$ 2.14 (s, 6H); 3.79−3.67 (m, 12H); 6.67 (s, 1H); 6.74 (s, 2H); 6.86−6.83 (m, 2H); 7.10−7.04 (t, 3H); 7.19 (s, 1H); 7.31−7.27 (m, 3H); 7.56−7.49 (dt, 3H); 8.50−8.47 (dt, 3H).

**2-[*N*-bis-(2-pyridylmethyl)aminomethyl]-4-methyl-6-[*N′*-(2-pyridylmethyl)(2-hydroxy-5-bromobenzyl)aminomethyl]phenol; H₂L-Br).** The ligand *N*-(2-hydroxy-5-bromobenzyl)(2-pyridylmethyl)amine (hbpa-Br) was obtained as follows: 2.01 g (10 mmol) of 2-hydroxy-5-bromobenzaldehyde was dissolved in 50 mL of toluene and was added dropwise to 1.49 mL of 2-(aminomethyl)pyridine (10 mmol) while stirring. The flask was equipped with a Dean−Stark trap and after 1 h of reflux, 0.37 g (10 mmol) of sodium borohydride was slowly added. The pH was then adjusted to 6.0 using 2.0 mol $L^{-1}$ HCl. The solution was washed with a saturated sodium bicarbonate ($3 \times 50$ mL), dried over $Na_2SO_4$, filtered off, and the solvent evaporated under reduced pressure. A 2.93 g portion (10 mmol) of hbpa-Br was obtained as a pale yellow oil. Yield: 99%; IR (KBr) in $cm^{-1}$: $\nu$(N−H) 3435; $\nu$(C−H$_{ar}$ and C−H$_{aliph}$) 3062−2851; $\nu$(C=N and C=C) 1592−1477; $\nu$(C−O) 1267; $\delta$(C−H$_{ar}$) 763; ^{1}H NMR, $\delta_H$ (200 MHz; CDCl₃), in ppm: 3.91 (s, 4H); 6.74−7.67 (m, 6H); 8.58 (d, 1H).

The ligand H₂**L-Br** was synthesized by adding 1.60 g of hbpa-Br (5.46 mmol) and 2.1 mL of triethylamine (15 mmol) to a 50 mL $CH_2Cl_2$ solution containing 2.21 g of bpmamcf·HCl (5.46 mmol).[7] After reflux for 72 h, the solution was cooled, washed with aqueous sodium bicarbonate solution, dried over anhydrous sodium sulfate, and the solvent removed under vacuum. The oil remaining was dried in a vacuum desiccator (0.1 mmHg) for 6 h, and 2.39 g of a yellow oil was obtained. Yield: 70%; IR (KBr) cm$^{-1}$: $\nu$(C−H$_{Ar}$ and C−H$_{aliph}$) 3056−2820; $\nu$(C=C and C=N) 1592−1480; $\delta$(O−H) 1368; $\nu$(C−O$_{phenol}$) 1262; $\nu$(C−H$_{Ar}$) 758; ^{1}H NMR (200 MHz; CDCl₃): $\delta$ 2.19 (s, 3H); 3.86 (s, 8H); 3.92 (s, 2H); 3.97 (s, 2H); 6.73−7.21 (m, 7H); 7.33−7.42 (m, 4H); 7.60−7.64 (t, 3H); 8.57 (d, 3H).

**Preparation of Complexes. *Caution!*** *Perchlorate salts of metal complexes are potentially explosive and therefore should be prepared in small quantities.*

(22) It should be noted that under certain circumstances (i.e., depending on the metal ion composition and type of substrate used in assays) PAPs may employ an alternative mechanism in which the substrate forms an initial $\mu$-1,3 phosphate complex prior to hydrolysis, thus placing the $\mu$-(hydr)oxo bridge in an ideal position to act as the reaction initiating nucleophile.[2,11,12]

(23) Cox, R. S.; Schenk, G.; Mitic, N.; Gahan, L. R.; Hengge, A. C. *J. Am. Chem. Soc.* **2007**, *129*, 9550−9551.

(24) Schenk, G.; Gahan, L. R.; Carrington, L. E.; Mitic, N.; Valizadeh, M.; Hamilton, S. E.; de Jersey, J.; Guddat, L. W. *Proc. Natl. Acad. Sci. U.S. A.* **2005**, *102*, 273−278.

(25) Smoukov, S. K.; Quaroni, L.; Wang, X.; Doan, P. E.; Hoffman, B. M.; Que, J. L. *J. Am. Chem. Soc.* **2002**, *124*, 2595−2603.

(26) Bunton, C. A.; Farber, S. J. *J. Org. Chem.* **1969**, *34*, 767−772.

(27) Gagné, R. R.; Farber, S. J. *J. Org. Chem.* **1980**, *19*, 2854−2855.

(28) Carvalho, M. L.; Santhiago, M.; Peralta, R. A.; Neves, A.; Micke, G. A.; Vieira, I. C. *Talanta* **2008**, *77*, 394−399.

**[Fe^{III}Zn^{II}(L-CH_3)(μ-OH)(H_2O)](ClO_4)_2·2.5H_2O (1).** To a 60 mL methanol solution of $H_2L-CH_3$ (0.28 g, 0.5 mmol) was added with stirring 0.19 g (0.5 mmol) of $Zn(ClO_4)_2·6H_2O$. To this solution was added dropwise a methanol solution (60 mL) of $Fe(ClO_4)_3·9H_2O$ (0.26 g, 0.5 mmol) and 3 mmol of NaOH in 6.5 mL of water. The stirring was maintained for approximately 15 min and then $NaClO_4$ (0.12 g, 1 mmol) was added. The solution was filtered off and left to stand. The resulting blue product was collected and washed with water and diethyl ether (Yield: 0.26 g, 55%). Single crystals suitable for X-ray analysis were obtained after recrystallization from methanol. Anal. Calcd for $C_{35}H_{43}Cl_2N_5O_{14.5}FeZn$: C: 43.88; H: 4.53; N: 7.31. Found: C: 43.71; H: 4.27; N: 7.34%. IR (KBr), cm$^{-1}$: $\nu$(OH) 3426; $\nu$(C-H$_{Ar}$ and C-H$_{aliph}$) 3039-2861; $\nu$(C=N and C=C), 1610-1437; $\nu$(C-O) 1276; $\nu$(Cl-O) 1097; $\delta$(C-H$_{Ar}$) 767.

**[Fe^{III}Zn^{II}(L-H)(μ-OH)(H_2O)](ClO_4)_2·H_2O (2). (2)** was prepared as described previously.[14]

**[Fe^{III}Zn^{II}(L-Br)(μ-OH)(H_2O)][ClO_4]_2·H_2O (3).** To a 60 mL methanol solution of $H_2L-Br$ (0.31 g, 0.5 mmol; 624.58 g·mol$^{-1}$) was added with stirring $Zn(ClO_4)_2·6H_2O$ (0.19 g, 0.5 mmol) and 3 mmol of NaOH in 6.5 mL of water. To this solution was added dropwise a methanol solution (60 mL) of $Fe(ClO_4)_3·9H_2O$ (0.26 g, 0.5 mmol). The solution was heated and stirred for 15 min. $NaClO_4$, (0.12 g, 1 mmol) was added, and the solution left to sit at room temperature. After about 15 min a purple precipitate formed which was filtered and washed with water and cold ether (0.30 g, 55% yield). After recrystallization from methanol, microcrystals were obtained. Anal. Calcd for $FeZnC_{34}H_{35}BrN_5O_5$-$(ClO_4)_2·H_2O$, C, 41.01; H, 3.75; N, 7.03%. Found: C, 40.95; H, 3.95; N, 7.23%. IR (KBr), cm$^{-1}$: $\nu$(OH) 3395; $\nu$(C-H$_{Ar}$ and C-H$_{aliph}$) 3058-2880; $\nu$(C=N and C=C) 1609-1437; $\nu$(C-O) 1282; $\nu$(Cl-O) 1101; $\delta$(C-H$_{Ar}$).

**[Fe^{III}Zn^{II}(L-NO_2)(μ-OH)(H_2O)][ClO_4]_2·H_2O (4).** To a 60 mL methanol solution of $H_2L-NO_2$ (0.30 g, 0.5 mmol; 590.70 g·mol$^{-1}$) was added with stirring and heating $Zn(ClO_4)_2·6H_2O$ (0.19 g, 0.5 mmol). To this solution was added dropwise a methanol solution (60 mL) of $Fe(ClO_4)_3·9H_2O$ (0.26 g, 0.5 mmol) and 3 mmol of NaOH in 6.5 mL of water. The solution was heated and stirred for 15 min. $NaClO_4$, (0.12 g, 1 mmol) was added, and the solution left to sit at room temperature. After about 15 min a red precipitate formed which was filtered and washed with water and ether (0.29 g, 60% yield). Single crystals suitable for X-ray structural analysis were obtained after recrystallization from methanol. Anal. Calcd for $FeZnC_{34}H_{35}N_6O_6(ClO_4)_2·H_2O$, C, 42.45; H, 3.89; N, 8.74%. Found: C, 41.90; H, 4.04; N, 8.53%. IR (KBr), cm$^{-1}$: $\nu$(OH) 3400; $\nu$(C-H$_{Ar}$ and C-H$_{aliph}$) 3063-2864; $\nu$(C=N and C=C) 1607-1440; $\nu$(N-O) 1292; $\nu$(C-O) 1292; $\nu$(Cl-O) 1091; $\delta$(C-H$_{Ar}$) 770.

**[Fe^{III}Zn^{II}(L-H)(μ-OAc)_2][ClO_4]_2·H_2O (5). (5)** was prepared as described previously.[9]

**Electron Paramagnetic Resonance (EPR) Spectroscopy.** EPR spectra were collected with a Bruker Elexsys E500 continuous wave spectrometer fitted with an X-band Super HighQ cavity. A Bruker ER 035 M Gaussmeter and an EIP 548B microwave frequency counter were used for calibration of the magnetic field and microwave frequency. Low temperatures (2 K) were obtained using an Oxford ESR910 flow through cryostat in conjunction with an Oxford instruments ITC-4 temperature controller. Bruker's Xepr (v2.2b.38) software was used for spectrometer tuning, signal averaging, and plotting. Computer simulations of the collected data were performed using the XSophe-Sophe-XeprView computer simulation software suite (v1.1.4).[29]

**Magnetic Circular Dichoism (MCD) Spectroscopy.** Spectra were acquired using a Lastek Pty. Ltd. developed instrument[30]

consisting of a Jobin/Yvon 750S monochromator, calcite polarizer, a Hinds PEM90 photoelastic modulator, an Oxford Instruments SpectroMag 7T superconducting magnet with an Hamamatsu S5 photomultiplier. The total and differential circularly polarized light from a 250 W halogen lamp at reference frequencies of the modulator and a New Focus 7051 optical chopper were detected using Stanford SR830 lockin amplifiers, allowing the simultaneous measurement of absorbance and MCD. Samples were dissolved in a glassing solution of MeOH:EtOH (1:2) to concentrations of about 1.5 mM, and the spectra were acquired using 1 mm path length quartz cells.

**Potentiometric Titration.** The potentiometric studies were carried out with a Micronal B375 pH meter fitted with blueglass and calomel reference electrodes calibrated to read $-\log[H^+]$ directly, designated as pH. Doubly distilled water in the presence of $KMnO_4$ and reagent grade ethanol were used to prepare the ethanol/water (70/30, v/v) solutions. The electrode was calibrated using the data obtained from a potentiometric titration of a known volume of a standard 0.100 M HCl solution with a standard 0.100 M KOH solution. The ionic strength of the HCl solution was maintained at 0.100 M by addition of KCl. The measurements were carried out in a thermostatted cell containing a solution of the complex (0.05 mol/50 mL) with ionic strength adjusted to 0.100 M by addition of KCl, at 25.00 $\pm$ 0.05 °C. The experiments were performed under an argon flow to eliminate the presence of atmospheric $CO_2$. The samples were titrated by addition of fixed volumes of a standard $CO_2$-free KOH solution (0.100 M). An ethanol/water (70/30 v/v) solution was chosen as the medium for the potentiometric titrations because of the low solubility of complexes in water. The p$K_w$ of the mixture ethanol/water 70/30 v/v containing 0.100 M KCl was 14.72(2).[31] The deprotonation constants were calculated using the BEST7 program[32] and species distribution were made using SPE and SPEPLOT programs.[32]

**Single-Crystal X-ray Structure Determinations.** Crystallographic analyses of complexes **1** and **4** were carried out with an Enraf-Nonius CAD4 diffractometer with graphite-monochromated Mo-K$_\alpha$ radiation ($\lambda$ = 0.71069 Å), at room temperature. Cell parameters were determined from 25 carefully centered reflections using a standard procedure.[33] Intensities were collected using the $\omega$-2$\theta$ scan technique. All data were corrected for Lorentz and polarization effects.[34] An empirical absorption correction based on the azimuthal scans of 7 appropriate reflections was also applied to the collected intensities using the PLATON program.[35] The structures were solved by direct methods and refined by full-matrix least-squares methods using the SHELXS97[36] and SHELXL97[37] programs, respectively. H atoms attached to C atoms were placed at their idealized positions, with C-H distances and $U_{eq}$ values taken from the default settings of the refinement program. Complex **1**: an irregular block cut off from a big dark red crystal was selected and fixed at the end of a glass fiber for X-ray analysis. All non-hydrogen atoms were refined with anisotropic displacement parameters, except for oxygen atoms of the perchlorate counterions and water solvate, which were refined isotropically. H atoms of the water molecule of crystallization (O2W) could not

(29) Hanson, G.; Gates, K. E.; Noble, C. J.; Griffin, M.; Mitchell, A.; Benson, S. *J., Inorg. Biochem.* **2004**, *98*, 903.

(30) Riley, M. J.; Krausz, E. R.; Stanco, A. *J. Biol. Inorg. Chem.* **2003**, *96*, 217.

(31) Schwingel, E. W.; Arend, K.; Zarling, J.; Neves, A.; Szpoganicz, B. *J. Braz. Chem. Soc.* **1996**, *7*, 31–37.

(32) Martell, A. E.; Montekaitis, R. J. *Determination and use of stability constants*, 2nd ed.; VCD: New York, 1992.

(33) *CAD4 EXPRESS*, ver 5.1/1.2; Enraf-Nonius: Delft, The Netherlands, 1994.

(34) Spek, A. L. *HELENA: CAD-4 data reduction program*; University of Utrecht: The Netherlands, 1996.

(35) Spek, A. L. *PLATON: molecular geometry and plotting program*; University of Utrecht: The Netherlands, 1997.

(36) Sheldrick, G. M. *SHELXS97: program for the solution of crystal structures*; University of Göttingen: Göttingen, Germany, 1990.

(37) Sheldrick, G. M. *SHELXL97: program for the refinement of crystal structures*; University of Göttingen: Göttingen, Germany, 1997.

be located. H atoms of the coordinated water and hydroxo bridge were found from a Fourier difference map and treated with a riding model. The oxygen atoms of the perchlorate counterions were found to be disordered over two alternative positions, and their refined site occupancies were 0.55(4) and 0.45(4). Complex **4**: the crystallographic data were acquired from a selected irregular block cut off from a large dark red crystal taken from the crystalline sample. The crystals of this complex showed low scattering power. From 6251 poorly diffracted reflections, only 2572 reflections were observed with $I > 2\sigma$. However, non-H atoms could be refined with anisotropic displacement parameters, except for oxygen atoms of the perchlorate counterions and water solvate. Hydrogen atoms of the water molecules and hydroxo bridge were not found in the Fourier map. Further relevant crystallographic data for complexes **1** and **4** are summarized in Supporting Information, Table S1.

**Theoretical Calculations.** The geometry optimization of the four cationic complexes **1**−**4** was performed using the B3LYP hybrid density functional theory in combination with the 6-31G(d, p) and LACVP* basis sets using Gaussian03.[38,39] To ensure that the geometry was minimized, a frequency calculation was performed (B3LYP, LANL2DZ), finding only one weak, low energy imaginary frequency corresponding to a minor rotatory vibration of the methyl group.

**Kinetic Assays for Complexes.** Phosphodiesterase-like activity was determined for complexes **1**−**4** by measuring hydrolysis of the substrate bis-(2,4-dinitrophenyl)phosphate (2,4-bdnpp) in an UV−vis Varian Cary 50 BIO spectrometer. The data were accompanied by monitoring the release of 2,4-dinitrophenolate at 400 nm. The rates were measured in real time at various pH values, and the extinction coefficients of the product 2,4-dinitrophenolate were measured at different pH's under the same experimental conditions of the kinetic measurements at different pH's/($\lambda = 400 \text{ nm}/\varepsilon$, $M^{-1} \text{ cm}^{-1}$) (3.5/2125; 4.0/3410; 4.5/7180; 5.0/10080; 5.5/11400; 6.0/12,000; 6.5−10.0/12,100). Reactions were monitored to less than 5% of conversion of substrate to product, and the data were treated by the initial rate method. The effect of pH on the rate of hydrolysis of 2,4-bdnpp between pH 3.6 and 10.25 (buffers - MES; HEPES and CHES 0.05 mol $L^{-1}$) was investigated by using fixed concentrations of substrate ([S]$_{final}$ = 5 × $10^{-3}$ mol $L^{-1}$), and complex ([C]$_{final}$ = 4 × $10^{-5}$ mol $L^{-1}$ for complexes **1** and **3** and 4 × $10^{-5}$ mol $L^{-1}$ for complex **4**), with excess of substrate at 25 °C ($I$ = 0.05 mol $L^{-1}$ with LiClO$_4$). Substrate dependence ([S]$_{final}$ = 5 × $10^{-4}$−7 × $10^{-3}$ mol $L^{-1}$) of the catalytic rate was measured at the optimum pH for each complex. The data were treated using the Michaelis−Menten non-linear regression ($V_0$ vs [bdnpp]). Isotopic effects of deuterium on the hydrolysis of 2,4-bdnpp promoted by complexes **1**, **3**, and **4** were investigated monitoring parallel reactions, where the buffer solutions MES pH and pD 6.50 were prepared in H$_2$O and D$_2$O, respectively to determine the relation

$k_H/k_D$.[14] The reactions were monitored under a 125-fold excess of substrate at 400 nm for complexes **1**, **3**, and **4**.

**Preparation of Plasmid DNA.** Plasmid DNA pBSK II (Stratagene) was obtained and purified according to standard techniques.[40,41] Briefly, *Escherichia coli* DH5alpha cells were transformed with pBSK II. One colony was incubated overnight in 5 mL of Lysogeny broth (LB) medium medium[42,43] supplemented with 0.1 mg/mL of ampicillin at 37 °C with aeration; and then 1 mL was inoculated in 300 mL of LB medium supplemented with 0.1 mg/mL of ampicillin and incubated for 8 h at 37 °C with aeration. From these cultures plasmid DNA was purified using Qiagen Plasmid Maxi Prep Kit. DNA was quantified by spectrophotometry using the ratio of the absorbance at 260 and 280 nm.[40] The plasmid preparation was analyzed by gel electrophoresis to ensure that it consisted of approximately 90% intact supercoiled plasmid DNA.

**DNA Cleavage Activity Assays.** The ability of **1**−**4** to cleave DNA was examined by following the conversion of supercoiled plasmid DNA (F I) to open circular DNA (F II) or linear DNA (F III) using agarose gel electrophoresis to separate the cleavage products.[41,44]

In general, 400 ng of pBSK II (~30 mmol $L^{-1}$ bp) buffered with PIPES (10 mmol $L^{-1}$, pH 6.5) were treated with **1**−**4** in CH$_3$CN (25% reaction volume) for different time reactions at 50 °C. Thereafter, each reaction was quenched adding 5 $\mu$L of a loading buffer solution (0.25% bromophenol blue, 50% glycerol and 250 mmol $L^{-1}$ ethylenediamine tetraacetic acid (EDTA) at pH 8.0) and then subjected to electrophoresis on a 0.8% agarose gel containing 0.3 mg mL$^{-1}$ of ethidium bromide in 0.5x TBE buffer (44.5 mmol $L^{-1}$ TRIS, 44.5 mmol $L^{-1}$ boric acid and 1 mmol $L^{-1}$ EDTA) at 90 V for approximately 1.5 h. The resulting gels were visualized and digitized using a DigiDoc-It gel documentation system (UVP, U.S.A.). The proportion of plasmid DNA in each band was quantified using KODAK Molecular Imaging Software 5.0 (Carestream Health, U.S.A.). The portion of supercoiled DNA (F I) was corrected by a factor of 1.47,[45] since the ability of ethidium bromide to intercalate into this DNA topoisomeric form is decreased relative to open circular and linear DNA. To elucidate whether the mechanism of DNA cleavage performed by complexes **1**−**4** is hydrolytic or oxidative, different inhibitors of reactive oxygen species (ROS) were added to the DNA treatments prior to the complexes. These inhibitors were dimethyl sulfoxide (DMSO, 10%), KI (500 mmol $L^{-1}$), superoxide dismutase (SOD, 15 Units), and NaN$_3$ (500 mmol $L^{-1}$). In addition, assays in the presence of DNA minor groove binder distamycin[46] (50 $\mu$mol $L^{-1}$) and the DNA major groove binder methyl green[47] (50 $\mu$mol $L^{-1}$) were also performed to clarify the DNA groove binding preference of the complex-DNA interaction. The plasmid DNA was pretreated with distamycin and methyl green for 30 min and then treated with the complex as described above. The kinetics of plasmid DNA cleavage performed by **1**−**4** were evaluated following the loss of supercoiled DNA fraction along the

(38) Becke, A. D. *J. Chem. Phys.* **1993**, *98*, 5648–5652.
(39) Frisch, M. J.; Trucks, G. W.; Schlegel, H. B.; Scuseria, G. E.; Robb, M. A.; Cheeseman, J. R.; J. A. Montgomery, J.; Vreven, T.; Kudin, K. N.; Burant, J. C.; Millam, J. M.; Iyengar, S. S.; Tomasi, J.; Barone, V.; Mennucci, B.; Cossi, M.; Scalmani, G.; Rega, N.; Petersson, G. A.; Nakatsuji, H.; Hada, M.; Ehara, M.; Toyota, K.; Fukuda, R.; Hasegawa, J.; Ishida, M.; Nakajima, T.; Honda, Y.; Kitao, O.; Nakai, H.; Klene, M.; Li, X.; Knox, J. E.; Hratchian, H. P.; Cross, J. B.; Adamo, C.; Jaramillo, J.; Gomperts, R.; Stratmann, R. E.; Yazyev, O.; Austin, A. J.; Cammi, R.; Pomelli, C.; Ochterski, J. W.; Ayala, P. Y.; Morokuma, K.; Voth, G. A.; Salvador, P.; Dannenberg, J. J.; Zakrzewski, V. G.; Dapprich, S.; Daniels, A. D.; Strain, M. C.; Farkas, O.; Malick, D. K.; Rabuck, A. D.; Raghavachari, K.; Foresman, J. B.; Ortiz, J. V.; Cui, Q.; Baboul, A. G.; Clifford, S.; Cioslowski, J.; Stefanov, B. B.; Liu, G.; Liashenko, A.; Piskorz, P.; Komaromi, I.; Martin, R. L.; Fox, D. J.; Keith, T.; Al-Laham, M. A.; Peng, C. Y.; Nanayakkara, A.; ; Challacombe, M.; Gill, P. M. W.; Johnson, B.; Chen, W.; Wong, M. W.; Gonzalez, C.; Pople, J. A. *Gaussian 03*, Revision C.02; Gaussian Inc: Wallingford, CT, 2004.

(40) Ausubel, F. M.; Brent, R.; Kingston, R. E.; Moore, D. D.; Seidman, J. G.; Smith, J. A.; Struhl, K. In *Short protocols in molecular biology: A compendium of methods from current protocols in molecular biology*; Wiley: New York, 1999.
(41) Scarpellini, M.; Neves, A.; Horner, R.; Bortoluzzi, A. J.; Szpoganicz, B.; Zucco, C.; Silva, R. A. N.; Drago, V.; Mangrich, A.; Ortiz, W. A.; Passos, W. A. C.; de Oliveira, M. C. B.; Terenzi, H. *Inorg. Chem.* **2003**, *42*, 8353–8365.
(42) Bertani, G. *J. Bacteriol.* **2004**, *186*, 595–600.
(43) Bertani, G. *J. Bacteriol.* **1951**, *62*, 293–300.
(44) Neves, A.; Terenzi, H.; Horner, R.; Horn, A.; Szpoganicz, B.; Sugai, J. *Inorg. Chem. Commun.* **2001**, 388–439.
(45) Bernadou, J.; Pratviel, G.; Bennis, F.; Girardet, M.; Meunier, B. *Biochemistry* **1989**, *28*, 7268–7275.
(46) Hiraku, Y.; Oikawa, S.; Kawanishi, S. *Nucleic Acids Res. Suppl.* **2002**, *61*, 95–96.
(47) Kim, S. K.; Norden, B. *FEBS Lett.* **1993**, *315*, 61–64.

**Table 1.** Comparison of Theoretical and Crystallographic Structural Data[a]

| | −CH$_3$ (**1**) | | −H (**2**) | | −Br (**3**) | −NO$_2$ (**4**) | |
|---|---|---|---|---|---|---|---|
| | exp | calc | exp | calc | calc | exp | Calc |
| Fe−Zn | 3.0862(18) | 3.136 | 3.041 | 3.135 | 3.135 | 3.067(2) | 3.130 |
| Fe−O1 | 2.053(3) | 2.077 | 2.028 | 2.063 | 2.064 | 2.031(8) | 2.033 |
| Fe−O2 | 1.920(7) | 2.002 | 1.934 | 1.998 | 1.998 | 1.932(8) | 1.990 |
| Fe−O3 | 2.112(3) | 2.206 | 2.054 | 2.204 | 2.204 | 2.107(9) | 2.198 |
| Fe−O4 | 1.893(4) | 1.891 | 1.923 | 1.887 | 1.896 | 1.910(8) | 1.900 |
| Fe−N2 | 2.137(8) | 2.153 | 2.136 | 2.145 | 2.149 | 2.117(10) | 2.137 |
| Fe−N4 | 2.186(3) | 2.230 | 2.178 | 2.227 | 2.230 | 2.189(9) | 2.225 |
| Zn−O1 | 2.101(3) | 2.066 | 2.059 | 2.073 | 2.074 | 2.103(8) | 2.093 |
| Zn−O2 | 1.969(6) | 2.008 | 1.966 | 2.009 | 2.010 | 1.981(9) | 2.014 |
| Zn−N1 | 2.152(7) | 2.216 | 2.141 | 2.212 | 2.213 | 2.135(10) | 2.205 |
| Zn−N3 | 2.073(8) | 2.128 | 2.067 | 2.142 | 2.126 | 2.087(11) | 2.122 |
| Zn−N5 | 2.056(8) | 2.143 | 2.051 | 2.126 | 2.141 | 2.038(11) | 2.137 |
| | | | | | | | |
| Fe−O1−Zn | 95.96(13) | 98.40 | 96.14 | 98.55 | 98.51 | 95.8(3) | 98.68 |
| Fe−O2−Zn | 105.0(3) | 102.87 | 102.47 | 102.89 | 102.91 | 103.2(4) | 102.82 |
| Fe−O4−C41 | 125.9(4) | 131.92 | 123.43 | 131.51 | 131.41 | 125.1(8) | 129.75 |
| Zn−Fe−O4−C41 | −151.81 | −165.25 | −152.64 | −163.48 | −163.41 | −152.22 | −159.35 |
| Fe−O4−C41−C46 | −45.07 | −31.38 | −48.36 | −34.28 | −33.71 | −47.49 | −39.58 |
| Fe−O1−C14 | 128.5(4) | 131.40 | 134.03 | 131.66 | 131.73 | 134.5(7) | 132.28 |
| Fe−O1−C14−C13 | 12.77 | 22.35 | 6.70 | 21.80 | 21.46 | 9.46 | 19.96 |
| O1−Zn−N1 | 89.4(2) | 90.02 | 90.46 | 90.15 | 90.15 | 89.1(3) | 90.27 |
| O1−Zn−N3 | 124.4(2) | 130.20 | 124.49 | 130.02 | 129.84 | 125.0(4) | 129.31 |
| O1−Zn−N5 | 110.8(2) | 112.13 | 109.47 | 112.22 | 112.36 | 111.1(4) | 112.51 |
| O1−Zn−O2 | 77.9(2) | 79.36 | 78.45 | 78.94 | 78.95 | 78.4(3) | 78.13 |
| O2−Zn−N1 | 166.0(3) | 167.53 | 167.31 | 167.22 | 167.42 | 166.4(3) | 166.73 |
| O2−Zn−N3 | 101.4(3) | 101.94 | 100.18 | 101.86 | 102.08 | 102.3(4) | 101.96 |
| O2−Zn−N5 | 110.2(3) | 110.84 | 108.63 | 110.94 | 110.63 | 109.4(4) | 110.74 |
| N1−Zn−N3 | 80.8(3) | 79.86 | 80.93 | 79.99 | 80.02 | 80.3(4) | 80.32 |
| N1−Zn−N5 | 79.6(3) | 79.12 | 80.73 | 79.24 | 79.22 | 80.0(4) | 79.51 |
| N3−Zn−N5 | 120.6(3) | 113.44 | 122.67 | 113.69 | 113.72 | 119.6(4) | 114.36 |
| $\tau = (\alpha - \beta)/60$ | 0.69 | | 0.71 | | | 0.69 | |

[a] Bond lengths are in Å, and bond angles are in deg. The atomic numbering follows that given in Figure 2.

reaction time under pseudo-first-order conditions. The apparent plasmid DNA cleavage rates ($k_{obs}$) were obtained from the plot of ln[Supercoiled DNA (%)] versus time. The reaction conditions were as the same as described above.

**Cell Lines and Cultures.** K562 is a cell line of chronic myelogenous leukemia established from pleural effusion of a 53 year-old female in terminal blast crisis, which was purchased from the Rio de Janeiro Cell Bank (number CR083 of the RJCB collection). The GLC4 cell line was derived from pleural effusion of a patient with small cell lung carcinoma. The cell lines were cultured in suspension in RPMI 1640 supplemented with 10% fetal calf serum in a humidified atmosphere with 5% CO$_2$ at 37 °C. Both cultures were initiated at 10$^5$ cells/mL and grew exponentially to about 8 × 10$^5$ cells/mL in 3 days.

For cytotoxicity measurements, 1 × 10$^5$ cells/mL were incubated for 72 h in the absence and presence of various concentrations of tested compounds. Cell viability was checked by Trypan Blue exclusion. Cell number was determined by Coulter counter analysis. The sensitivity to the drug was evaluated by the concentration required to inhibit cell growth by 50%, the IC$_{50}$. The mean IC$_{50}$ ± SD was determined in three independent experiments each performed in duplicate.

## Results and Discussion

**Geometric and Electronic Structures of the Complexes. (a). Crystallography.** The H$_2$**L-H** ligand has been used to generate a large number of heterovalent dinuclear complexes with different metals ions together with auxiliary ligands to complete their coordination spheres.[6−14] Selected crystallographic structural data are given in the Supporting Information, Table S1 for complexes **1** and **4**. Bond lengths and angles are given in Table 1. The complete

structures of the compounds **2** and **5** have been previously published[9,14] but for comparison are shown in Figure 2 together with the structures of **1** and **4**. Because of low intensity and quality of the diffraction data it was not possible to completely refine the structure of **4**. However, the data are considered to be of sufficient quality to permit structural details to be elucidated. Unfortunately, attempts to obtain suitable crystals of complex **3** were unsuccessful. We have used the electronic structure calculations to supplement the limited crystallographic data.

The molecular structures of **1** and **4** (Figure 2) show that in the dinuclear [**L-R**(OH$_2$)Fe($\mu$-OH)Zn]$^{2+}$ unit the Fe$^{III}$ ion is facially coordinated by the hard tridentate pendant arm of the ligands **L-CH$_3$**$^{2-}$ (**1**) or **L-NO$_2$**$^{2-}$ (**4**) containing the amine (N4) and pyridine nitrogen (N2) and the phenolate oxygen (O4) atoms, while Zn$^{II}$ is coordinated by the soft side of the ligand through the amine (N1) and pyridine (N3, N5) nitrogen atoms. The bridging phenolate oxygen O1, the bridging hydroxo group (O2), and a terminal water molecule (O3) complete the octahedral N$_2$O$_4$ coordination of Fe$^{III}$, while the distorted trigonal bipyramid of Zn$^{II}$ ($t$ = 0.69 for **1** and **4**)[48] is complemented by the bridging phenolate (O1) and the hydroxo (O2) oxygen atoms. Complexes **1** and **4** are isostructural with the previously reported complex **2**.[14] The Fe-$\mu$-**OH** (1.920 Å for **1**, 1.934 Å for **2**, and 1.932 Å for **4**, respectively) and Zn-$\mu$-OH (1.969 Å for **1**, 1.966 Å for **2**, and 1.981 Å for **4**, respectively) distances in **1**, **2**, and **4** are quite similar, which are somewhat shorter

(48) Addison, A. W.; Rao, T. N.; Reedijk, J.; van Rijn, J.; Verschoor, G. C. *J. Chem. Soc., Dalton Trans.* **1984**, 1349−1356.
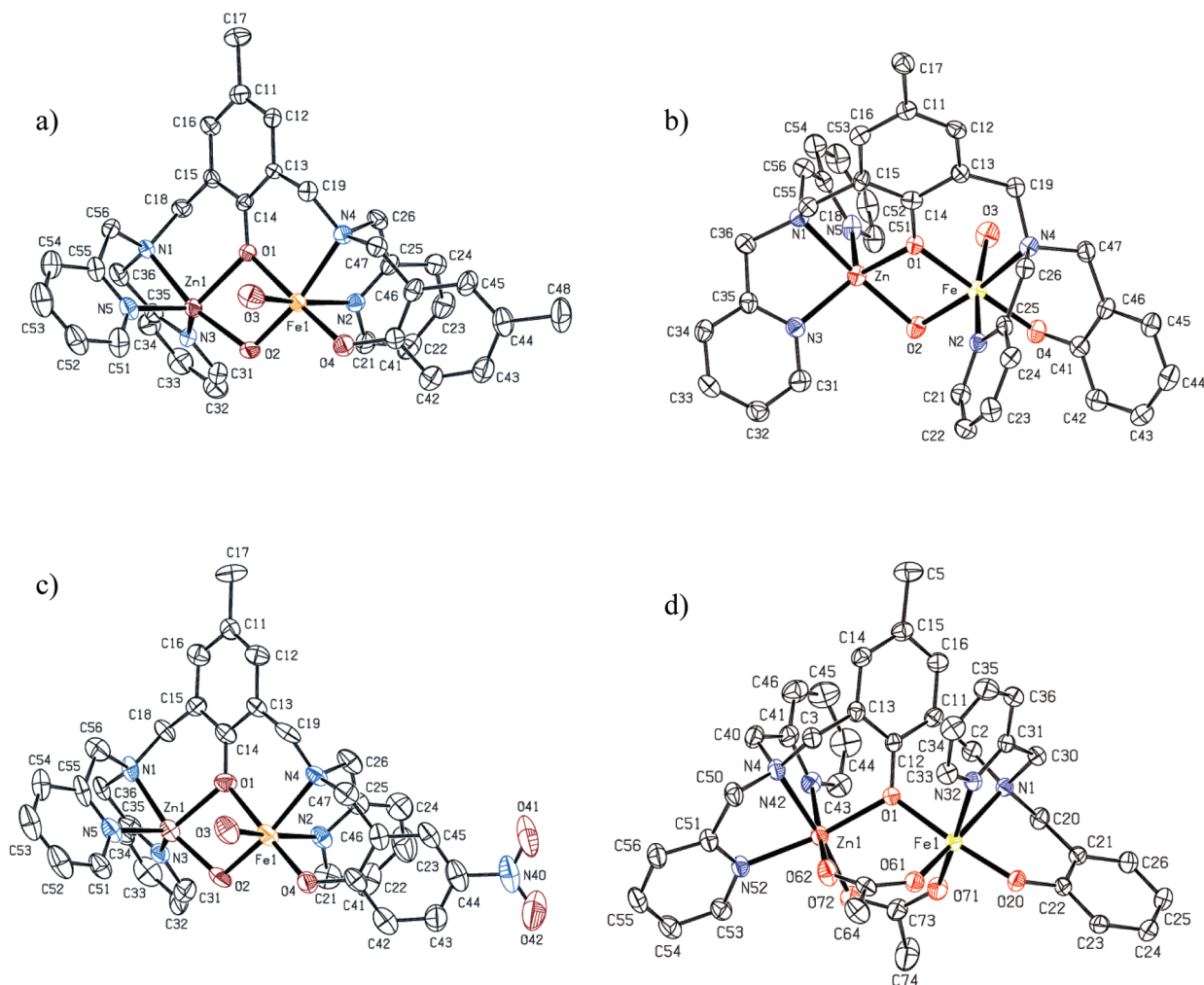
**Figure 2.** Crystal structures of (a) **1**, (b) **2**, (c) **4**, and (d) **5**.[9]

than the corresponding metal-$\mu$-OH distances in rkbPAP, which have been modeled between 2.0 and 2.2 Å.[1] Furthermore, the $Fe^{III}\cdots Zn^{II}$ distances (3.086 Å for **1**, 3.041 Å for **2**[14], and 3.067 Å for **4**) are shorter but comparable to the 3.20 Å found in rkbPAP. Importantly, the structures of **1**, **2**, and **4** reveal the presence of a terminal Fe-bound water molecule (Fe−O3 = 2.112 Å, 2.054 Å, and 2.107 Å, respectively), which occupies a position equivalent to that of one of the proposed nucleophiles in rkbPAP.[1,23]

Although the distinct substituents (−CH$_3$, −H, −NO$_2$) at the terminal $Fe^{III}$-bound phenolate do not cause any significant effect in the arrangement of the donor atoms around the metal centers and in the bond lengths and angles within this series of complexes, the same is not true regarding the physicochemical properties and reactivity of the complexes, as will be discussed below.

It is also of interest to compare the structure of the complex $[H_2OFe^{III}(\mu\text{-}OH)Zn^{II}(\textbf{L-H})]^{2+}$ (**2**)[14] with that of $[Fe^{III}Zn^{II}(\mu\text{-}OAc)_2(\textbf{L-H})]^+$ (**5**).[9] The complexes **2** and **5** are shown in Figure 3, the latter having diacetate bridges in a bidentate mode and the former a hydroxo bridge, with a terminal H$_2$O completing the coordination of the $Fe^{III}$ ion. In both cases the $Fe^{III}$ and $Zn^{II}$ ions are bridged by the phenolate oxygen of the **L-H**$^{2-}$ ligand (O1 in Figure 2), and the $Fe^{III}$ ion has the oxygen of the terminal phenolate (O4; Figure 2) bound in the position *trans* to

the bridging phenolate oxygen (O1). In the $\mu$-OAc complex (**5**) the $Fe^{III}$ ion is coordinated by the tertiary amine, pyridine and phenolate groups of the **L-H**$^{2-}$ ligand (facial arrangement) and the two bridging acetates to complete a $cis$-N$_2$O$_4$ coordination. The $Zn^{II}$ ion of the $\mu$-OAc complex is also six coordinate, with a $fac$-N$_3$O$_3$ coordination. Figure 3 shows the structural changes that accompany the change of the bridging acetates to a bridging hydroxide. Figure 3a shows **5** viewed in the directions perpendicular (upper) and parallel (lower) to a pseudo $C_2$ axis of the dimer that bisects the Fe−O1−Zn bridging angle, while Figure 3b shows the analogous views of complex **2**.

In complex **2** the $Fe^{III}$ ion retains the $cis$-N$_2$O$_4$ coordination, with a bridging hydroxide and a terminally bound water replacing the bridging acetates (Figure 3b). The $Zn^{II}$ ion in **2**, however, has a 5-fold N$_3$O$_2$ coordination. The $Fe^{III}$−$Zn^{II}$ distances (3.040 Å for **2** and 3.491 Å for **5**) bracket the value of 3.1 Å measured in rkbPAP in the presence of a sulfate ion that has been assumed to mimic the initial substrate binding mode in the outer coordination sphere,[4,5] and 3.5 Å in the presence of a metal ion bridging phosphate.[1] The $Fe^{III}$−O1 bond lengths are 2.028 Å (**2**) and 2.006 Å (**5**), while the $Fe^{III}$−O4 bonds to the terminal phenolate *trans* to O1 are considerably shorter (1.923 Å (**2**) and 1.890 Å (**5**)). As shown in Figure 3b complex **2** does not have the pseudo-$C_2$ symmetry seen in **5**. The change can
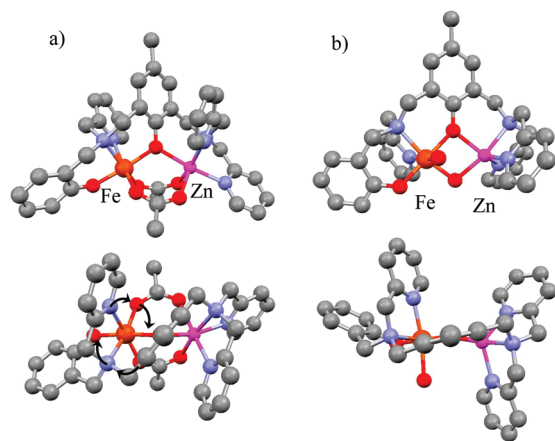
**Figure 3.** Comparison of the structures of **5** ($\mu$-OAc)$_2$(a, top/bottom) and **2** ($\mu$-OH) (b top/bottom) perpendicular and parallel to the pseudo $C_2$ axis of the dimer that bisects the Fe−O1−Fe bridging angle. In addition to the $\mu$-phenoxo bridging ligand, **5** and **2** also contain ($\mu$-OAc)$_2$ and $\mu$-OH bridging ligands, respectively. Hydrogen atoms have been deleted for clarity. The arrows in (a) bottom indicates the rotation of the octahedron on going from **5** to **2** (see text). Note the loss of the pseudo-$C_2$ symmetry in **2** (b bottom) and the steric crowding of the aromatic groups.

be viewed as the Fe$^{III}$ octahedron rotating about the R-phenolate-Fe-phenolate axis, such that the coordinate position of one of the acetate ligands moves to the bridging $\mu$-OH position as indicated by the arrows in Figure 3. This rotation causes the plane of the bridging phenolate to rotate to be almost within the Fe−O1−Zn plane, while in complex **5** it forms a 45° angle with that plane (compare bottom Figures 3a and 3b). This dramatic change also results in the tertiary amine rotating toward this plane with a concomitant shift of the attached pyridyl groups. The Zn coordination sphere undergoes a rotation in the opposite sense so that the coordinate positions *trans* to both the tertiary amines are directed to bind to the bridging OH$^-$ in **2**. The Fe−O1−Zn angle decreases from 116.2° to 96.1°, and the Fe−Zn distance decreases from 3.490 Å to 3.040 Å. The vacant position of the Fe$^{III}$ coordination sphere is occupied by a water molecule while that of the Zn$^{II}$ ion is accommodated by a distortion toward a five coordinate trigonal bipyramidal structure. The complex [Fe$^{III}$Zn$^{II}$($\mu$-OH)-(H$_2$O)**L-H**](ClO$_4$)$_2$ is the first structural model for PAPs with only one terminal phenolate, a $\mu$-hydroxo, and a molecule of water coordinated to the Fe$^{III}$.[14]

**(b). Electronic Structure Calculations.** The results for the geometry optimization of the complexes **1**−**4** are given in Table 1. A comparison between the available crystallographic (**1**, **2**, **4**) and calculated structural data sets shows good agreement. Small differences between the crystal data and the theoretical values are observed, and these can be assigned to the fact that the X-ray structures were measured in a compacted crystalline form whereas the calculations were performed in a vacuum, where crystal packing forces are absent.

Figure 4 shows a local coordinate system that we will use to describe the geometric environment of the Fe$^{III}$ ion and the effect on the energy of the d-orbitals. The $z$ axis is defined along the direction of the bridging and terminal phenolate ions, whose short bond lengths impart a tetragonally compressed geometry. The Fe$^{III}$Zn$^{II}$($\mu$-OH)(O1) core defines the yz plane, while the terminal water (O3) is approximately along the $x$ axis. The lower than tetragonal



$$E(xz) = \tfrac{1}{2}\,\pi(O4) + \pi(O1) + \pi(N2)$$
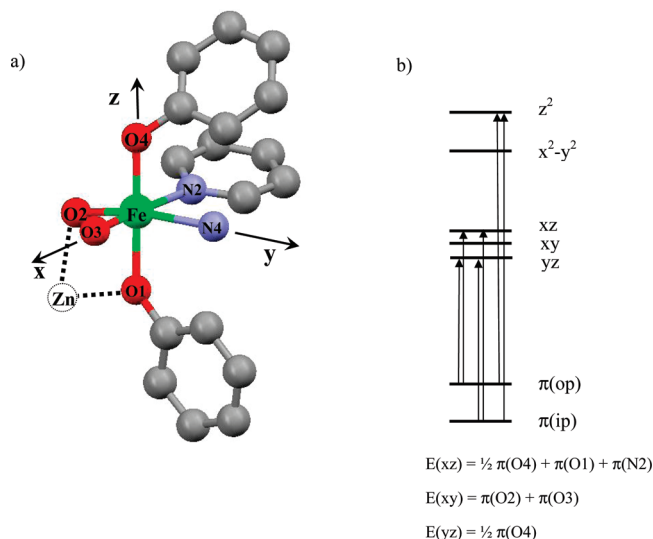$$E(xy) = \pi(O2) + \pi(O3)$$
$$E(yz) = \tfrac{1}{2}\,\pi(O4)$$

**Figure 4.** (a) Orientation of the molecular axes and aromatic planes for the Fe$^{III}$ center in **2** and (b) the relevant transitions and the energy expressions for the t$_{2g}$ orbitals, having an energy ~20,000 cm$^{-1}$. Energies for the e$_g$ orbitals is ~30,000 cm$^{-1}$.

symmetry of Fe$^{III}$ will remove the otherwise degenerate $xz$, $yz$ orbitals. As discussed below, the aromatic planes of the phenol and pyridine groups orient the anisotropic $\pi$ bonding of the ligating atoms. The energy of the d-orbitals will be affected by interactions mainly with the out-of-plane $\pi$-bonding orbitals of the aromatic groups, rather than with the in-plane orbitals, which will be lower in energy. In terms of the angular overlap model (AOM), it is the antibonding interaction with the donor ligand orbitals that raises the relative energy of the d-orbitals. From Figure 4a, for the O1 (phenolate) ligand, the out-of-plane p orbital will be approximately in the $xz$ plane, the N2 (pyridine) p orbital is approximately in the $xz$ plane, and for the O4 (terminal phenolate) ligand the $\pi$ bonding direction is defined by the torsional angles given in Table 1. The orientation of the O4 phenolate results in the out-of-plane (p$_{op}$) and in-plane (p$_{ip}$) p orbitals being able to participate in both $\sigma$- and $\pi$- bonding. From the location of the hydrogen atoms of the OH$^-$/H$_2$O ligands, the O2 (hydroxo bridge) and O3 (water) atoms are expected to mainly undergo $\pi$-bonding in the xy plane.

The angle formed by the terminal phenolate and the Fe$^{III}$ is 123.43°, 125.9°, and 125.1° (Fe−O4−C41, Table 1) for compounds **1**, **2**, and **4**, respectively, while the torsional angle of the phenolate plane with the Fe−O−C plane is 45.1°, 48.4°, and 47.5° (Fe−O4−C41−C46; Table 1). These values compare to the values 136° and 39° for the analogous angles in the tyrosine−Fe$^{III}$ bond in the Fe$^{III}$Zn$^{II}$ rkbPAP.[16] The close to 45° torsional angle results in the p$_{op}$ and p$_{ip}$ orbitals having mixed $\sigma$/$\pi$ bonding character and the $\pi$ bonding interactions of O4 are approximately equal with both $xz$ and $yz$ orbitals.

In six coordinate complexes, the ligand $\sigma$-bonding interactions are with the e$_g$ ($x^2-y^2$, $z^2$) orbitals only and the $\pi$-bonding interactions affects the t$_{2g}$ ($xy$, $xz$, $yz$) orbitals only. Using the orientations discussed above, and the approximation that the saturated N4 does not undergo $\pi$-bonding, the relative energy expressions of the t$_{2g}$ orbitals in terms of the AOM $\pi$ parameters are given in Figure 4b.
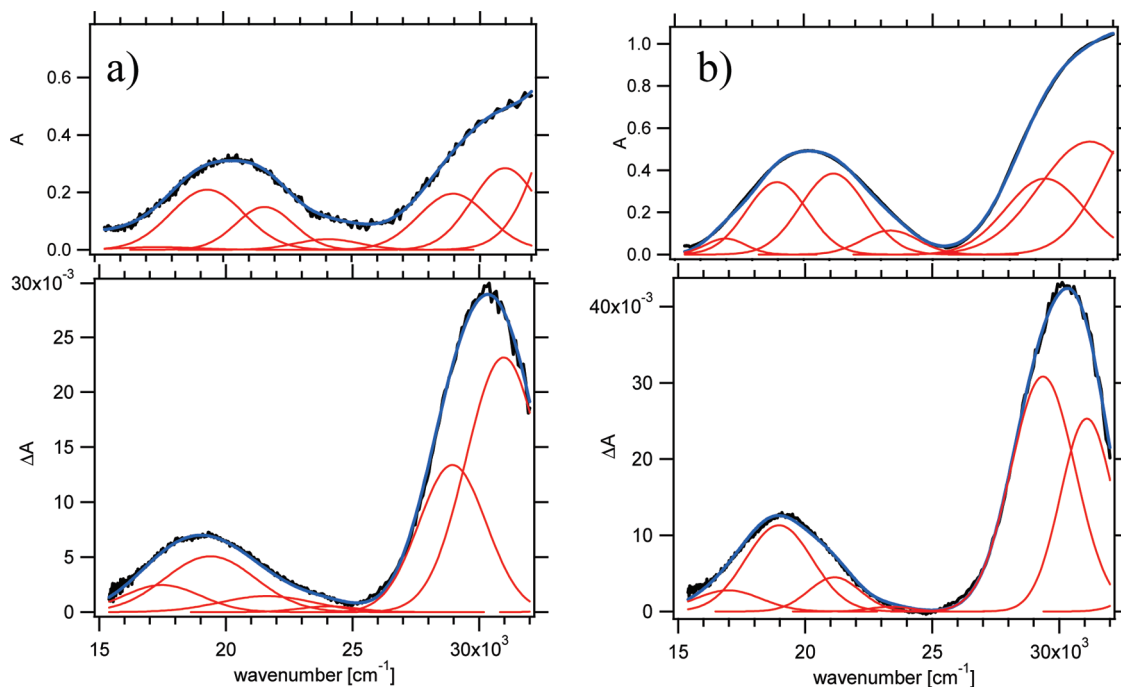
**Figure 5.** Illustrative absorption (top) and MCD (bottom) spectra of complexes **1** (a) and **2** (b) in a 1:1 methanol/ethanol at a temperature of 2 K and a magnetic field of 7 T.

**Table 2.** Energy of HOMO, Orbital Parameters, Electronic Absorption Spectral Analysis, Square Voltammetric Data, and Zero Field Splittings for Complexes **1−4**

| complex | $\sigma_p$ | $E_{HOMO}$ eV | $\lambda_{max}$ nm ($\varepsilon$ mol$^{-1}$ cm$^{-1}$)$^a$ | $E_{1/2}$ (mV vs NHE) | | $D$ cm$^{-1}$ ($E/D$) | |
|---|---|---|---|---|---|---|---|
| | | | | pH 3.5 | pH 6.5 | EPR | MCD$^b$ |
| **1** | −0.14 | −10.278 | 547(2195); 318(sh) | 57 | −197 | −1.0(0.18) | −0.7 |
| **2** | 0 | −10.485 | 544(2800) | 60 | −180 | 1.8(0.06) | 0.4 |
| **3** | 0.26 | −10.300 | 527 (1023) | 63 | −160 | | |
| **4** | 0.81 | −10.948 | 500(4047); 353(20700) | 70 | −100 | 4.0(0.065) | 0.8 |

$^a$ Solvent CH$_3$CN. $^b$ ($E/D$) values not fitted, taken from EPR.

In the low temperature absorption and MCD spectra of **1** and **2** (Figure 5) there are two groups of features at around 20,000 and 30,000 cm$^{-1}$ that correspond to LMCT transitions involving the charge transfer from a $\pi$ orbital on the terminal phenolate to the t$_{2g}$ and e$_g$ sets of the unfilled d orbitals of Fe$^{III}$, respectively. These transitions are a characteristic feature of PAPs and are responsible for these enzymes' purple color. The nature of the LMCT transitions in PAPs[16] and in the model [Fe$^{III}$Fe$^{II}$($\mu$-OAc)$_2$**L-H**]$^+$ complex have been established by MCD[17] and resonance Raman spectroscopy.[44] This leads to four expected transitions within the 20,000 cm$^{-1}$ band and two transitions within the 30,000 cm$^{-1}$ band in the phenolate−Fe$^{III}$ LMCT spectra as indicated in Figure 4b (only five of them are Gaussian resolved in Figure 5). The electronic spectra of complexes **1−4** in CH$_3$CN show the presence of two absorption maxima in the region 300−600 nm and the spectral data are summarized in Table 2. The lower and higher energy bands correspond to the p$\pi \rightarrow$ d$\pi^*$ and p$\pi \rightarrow$ d$\sigma$ phenolate to Fe$^{III}$ LMCT transitions discussed above.

**(c). Zero Field Splitting (ZFS) Parameters.** The energies of the d-orbitals in the Fe$^{III}$ d$^5$ system are also important for determining the sign and magnitude of the zero-field splitting (ZFS) parameters obtained from the EPR spectra. There are examples of Fe$^{III}$ with N/O donor sets that result in both high and low spin Fe$^{III}$ depending on the substituents and

steric effects.[49,50] This implies that these types of ligands are near the spin crossover region. While the present complexes **1−4** are all in the high spin configuration, there will be a close-lying quartet $^4$T$_{1g}$ excited state, and spin−orbit mixing is expected to generate relatively large ZFS values. The ZFS values of the $^6$A$_1$ ground state are determined by spin−orbit induced mixture with the excited $^4$T$_{1g}$ state when it is split by an orthorhombic low symmetry ligand field. From second order perturbation theory one finds[51]

$$D = \frac{\xi^2}{10}\left[\frac{2k_z^2}{E(^6A_1} \rightarrow {}^4T_{1z})} - \frac{k_y^2}{E(^6A_1} \rightarrow {}^4T_{1y})} \right.$$
$$\left. - \frac{k_x^2}{E(^6A_1} \rightarrow {}^4T_{1x})}\right] \quad (1)$$

$$E = \frac{\xi^2}{10}\left[\frac{k_y^2}{E(^6A_1} \rightarrow {}^4T_{1y})} - \frac{k_x^2}{E(^6A_1} \rightarrow {}^4T_{1x})}\right]$$

(49) Boča, R. *Struct. Bonding* (*Berlin*) **2006**, *117*, 1–264.
(50) Zang, Y.; Kim, J.; Dong, Y.; Wilkenson, E. C.; Appelman, E. H.; Que, J. L. *J. Am. Chem. Soc.* **1997**, *119*, 4197–4205.
(51) Abragam, A.; Bleaney, B. *Electron Paramagnetic Resonance of Transition Ions*; Dover: New York, 1986.
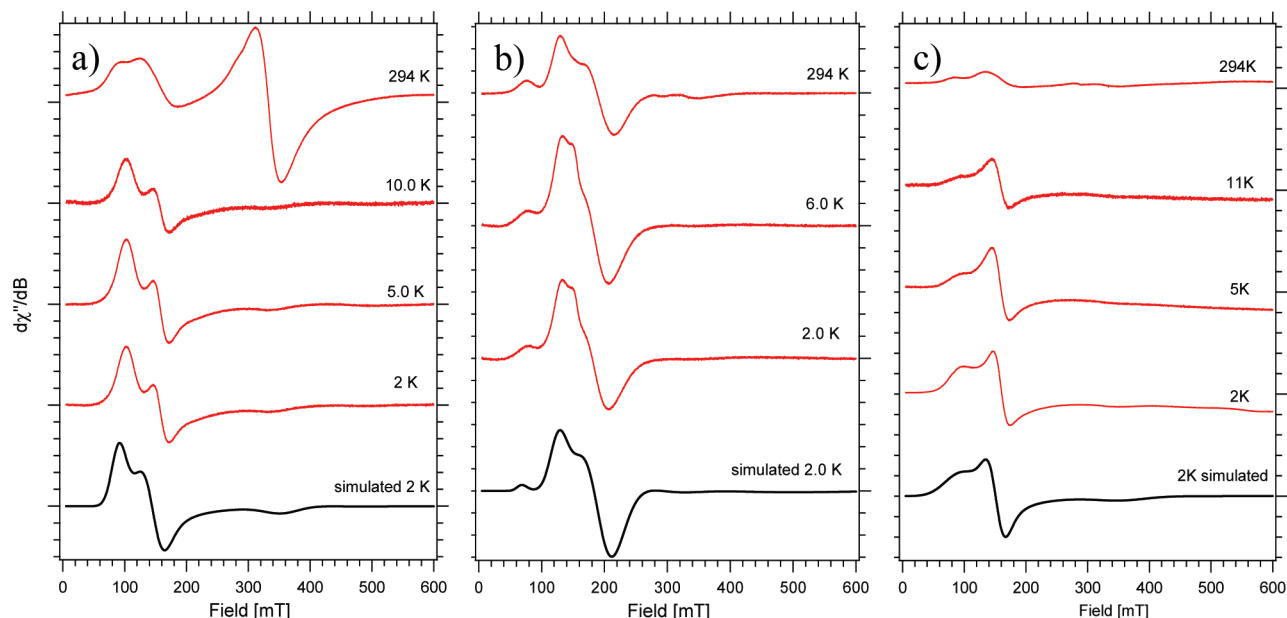
**Figure 6.** Experimental X-band EPR spectrum of complexes **1**, **2**, and **4** at the indicated temperatures in the solid state (microwave frequency 9.3499 GHz, microwave power 2 mW, modulation amplitude 0.1 mT, and receiver level 74 dB). The simulated spectra were made using the parameters given in the text (line width 400 G). The origin of the large signal at $g \sim 2$ that appears in the 294 K spectrum of **1** is unknown.

where $\xi$ is the spin−orbit coupling constant and $k_i$ are the orbital reduction factors, which are in general $\leq 1$. We have compared these expressions to those obtained from the full $d^5$ matrix diagonalization and find that they are in remarkably good agreement to within 5% over a range of parameters appropriate to this system. The relative energies of the split $^4T_{1g}$ components are to a good approximation determined by the relative energies of the $t_{2g}$ d-orbitals. Assuming isotropic orbital reduction factors, and taking into account that the average energy of the $^4T_{1g}$ components is given by the strong field expression $40B - \Delta_o$, where $\Delta_o$ is the overall effective octahedral splitting, then the above expressions reduce to

$$D = \frac{\xi^2 k^2}{10(40B - \Delta_o)^2}[2E(xy) - E(xz) - E(yz)]$$

$$= \frac{\xi^2 k^2}{5(40B - \Delta_o)^2}[\pi_x + \pi_y - 2\pi_z] \quad (2)$$

$$E = \frac{\xi^2 k^2}{10(40B - \Delta_o)^2}[E(xz) - E(yz)]$$

$$= \frac{\xi^2 k^2}{5(40B - \Delta_o)^2}[\pi_y - \pi_x]$$

in terms of the d-orbital energies $E(xy)$, $E(xz)$, $E(yz)$. The $\pi_x$, $\pi_y$ and $\pi_z$ parameters in the right-hand side expressions are isotropic $\pi$-bonding parameters for ligands along the x, y, and z axes. When evaluated for a tetragonal compression ($\pi_z > \pi_x = \pi_y$) the expected negative value for $D$ and a zero value for $E$ is obtained.

The above expressions demonstrate that it is the $\pi$-bonding which is the most important factor in determining the signs of the ZFS parameters. The $\sigma$-bonding contributes to the magnitude (but not the sign) of $D$ and $E$.

through the effective octahedral splitting $\Delta_o$ ($= 3\sigma - 4\pi$) in eq 2. Analogous expressions can be found for the specific anisotropic $\pi$-bonding pattern in the model complexes **1**−**4** as described above. Using the expressions for the relative energy of the $t_{2g}$ orbitals given in Figure 4b, together with eq 2 and typical values of $\Delta_o \sim 15{,}000\,\mathrm{cm}^{-1}$, $40B \sim 30{,}000\,\mathrm{cm}^{-1}$, $\zeta \sim 460\,\mathrm{cm}^{-1}$, and the values $k \sim 0.8$ and a common $\pi \sim 2000\,\mathrm{cm}^{-1}$ value.[52] The later value is taken as representative of N/O $\pi$ bonding.[53] Restriction of $|E/D| < 1/3$ requires the z→x permutation of the axes in Figure 4, giving $D = -0.66\,\mathrm{cm}^{-1}$ and $E = +0.094\,\mathrm{cm}^{-1}$. The surprising conclusion is that with this pattern of anisotropic $\pi$-bonding with a single common $\pi$ parameter, the principal axis of the ZFS parameters is perpendicular (not collinear) with the geometric axis of compression. That is, the principal axis of the ZFS parameters is along the N2−Fe−O3, not the O1−Fe−O4, direction. While it is not realistic to have a single $\pi$-bonding parameter, the above clearly shows the sensitivity of the ZFS parameters to the $\pi$- rather than the $\sigma$-bonding character of the ligands.

EPR spectra for complexes **1**, **2**, and **4** are shown in Figure 6, and the data were fitted to the following spin Hamiltonian, where standard axes are assumed to restrict the ZFS parameters to $E/D \leq 1/3$:

$$H_{spin} = \beta(g_x B_x \hat{S}_x + g_y B_y \hat{S}_y + g_z B_z \hat{S}_z)$$
$$+ D(\hat{S}_z^2 - 1/3S(S+1)) + E(\hat{S}_x^2 - \hat{S}_y^2) \quad (3)$$

While the g-values would be expected to have rhombic symmetry, in practice any anisotropy is very small[54] as the

(52) Lever, A. B. P. *Inorganic electronic spectroscopy*, 2nd ed.; Elsevier: New York, 1984.
(53) Figgis, B. N. Hitchman, M. A. *Ligand field theory and its applications*; Wiley-VCH: New York, 2000.
(54) Solomon, E. I.; Brunold, T. C.; Davis, M. I.; Kemsley, J. N.; Lee, S.-K.; Lehnert, N.; Neese, F.; Skulan, A. J.; Yang, Y.-S.; Zhou, J. *Chem. Rev.* **2000**, *100*, 235–349.
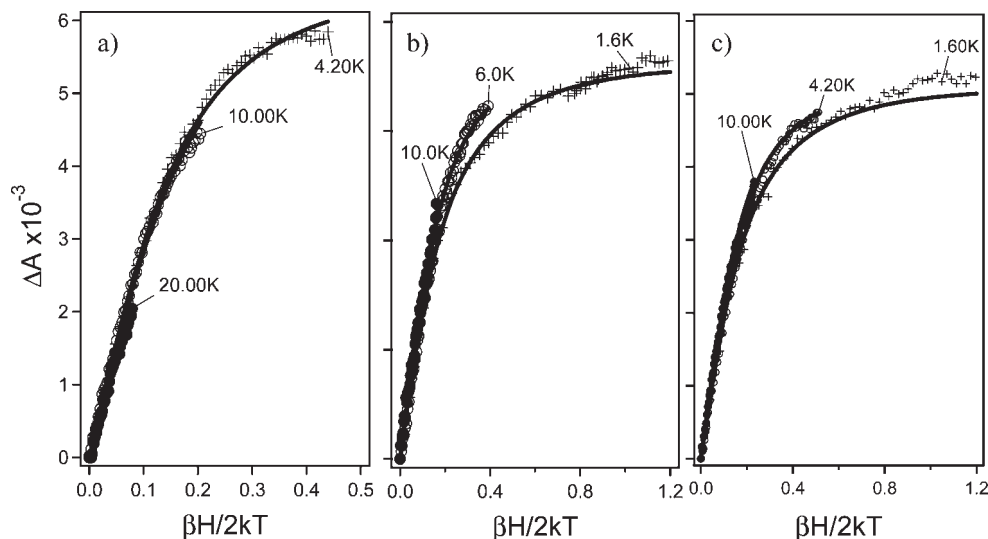
**Figure 7.** Fits of the VTVH MCD curves measured at 20,000 cm$^{-1}$ for the indicate temperatures. Panels (a)−(c) refer to samples **1, 2, 4**, respectively. Solid lines are fits using the parameters given in the text.

orbitally nondegenerate $^6A_{1g}$ ground state multiplet differs in spin multiplicity from all the excited ligand field states. On the other hand, the large effective $g$-values directly result from the action of the ZFS parameters (Supporting Information, Figures S1, S2). For this reason the ZFS parameters $D$ and $E$ are considered more useful in probing spectro-structural correlations in d$^5$ complexes using, for example, the simple perturbation expressions relating the ZFS parameters to AOM bonding parameters given in eq 2. The effective $g$-values, $g_{eff}$, are a sensitive function of $E/D$ as shown in the rhombogram in Supporting Information, Figure S2.

However, when the first excited quartet states are low in energy, the low-symmetry split components of the $^4T_{1g}$ excited state will be mixed into the $^6A_{1g}$ ground state multiplet to form "spin-admixed" states.[49] A way of incorporating the effect of this admixture within the spin Hamiltonian formalism is to use higher order terms (eq 4).[51]

$$H_{spin}^4 = \frac{a}{6}\{(\hat{S}_x^4 + \hat{S}_y^4 + \hat{S}_z^4) - 7/4(3\hat{S}^2 + 3\hat{S} + 1)\} \quad (4)$$

where the fine structure constant $a$ is defined in terms of the spin−orbit levels given in Supporting Information, Figure S1.

Since the crystal structures show that the closest intermolecular $Fe^{III}$−$Fe^{III}$ distance between different dimers is large (7.29 Å in **2**), the dipole−dipole interaction, which is proportional to $1/r^3$, will be significantly smaller than the ZFS and will generally result in dipolar broadening of the EPR resonances.[55] A dipole−dipole broadened spectrum was observed for **3** (results not shown). The low temperature EPR spectra have been simulated with isotropic $g$-values and the following ZFS parameters: $D = -1.0$ cm$^{-1}$; $E/D = 0.18$ (**1**); $D = +1.8$ cm$^{-1}$; $E/D = 0.06$ (**2**); and $D = +4.0$ cm$^{-1}$; $E/D = 0.065$ (**4**). In all cases the fits were improved by allowing the $g$-values to optimize to values between 1.85−2.0. It is unusual for the $g$-values in a d$^5$ system to depart appreciably from 2.0, and it would indicate

strong mixing with the excited state quartet, as do the relatively large ZFS parameters. The inclusion of the higher order terms in the spin Hamiltonian eq 4 improves the fits, but the additional parametrization makes it difficult to find a unique set.

The variable temperature variable field (VTVH) MCD data are given in Figure 7. The simulation of the VTVH MCD data was made using the formalism of Neese and Solomon[56] where, within a scaling factor $K$, the MCD magnetization curves are calculated as:

$$\frac{\Delta \varepsilon}{E} = K \int_0^\pi \int_0^{2\pi} \sum_i N_i (l\langle S_{xi}\rangle M_{yz}^{eff} + m\langle S_{yi}\rangle M_{xz}^{eff}$$
$$+ n\langle S_{zi}\rangle M_{xy}^{eff}) \sin\theta \, d\theta \, d\phi \quad (5)$$

where the summation is over the six $S = 5/2$ levels, and $N_i$ are the Boltzmann populations of the energy levels; $\langle S_{xi}\rangle$ is the expectation value of the spin $\hat{S}_x$ operator in level $i$, and $l$, $m$, and $n$ specify the direction cosines of the magnetic field with respect to a fixed molecular axis system with $l = \sin\theta \sin\phi$, $m = \sin\theta \cos\phi$, and $n = \cos\theta$. The parameters $M_{xy}^{eff}$, $M_{xz}^{eff}$, $M_{yz}^{eff}$ are the effective transition dipole moments that are treated as phenomenological parameters. In principle, these moments can be related to the intensities of particular transitions, but as there are many contributions this must be done on a case by case basis. In this particular case, the $z$ polarized nature of the transition (Figure 4) implies that $M_{xy}^{eff} < M_{xz}^{eff} = M_{yz}^{eff}$, and we have set these values to 0.1, 1.0, 1.0, respectively. The integration in eq 5 is done numerically, and the energy levels and wave functions are found by solving the ground state spin Hamiltonian given in eq 3. From the six energy levels and wave functions of the $|S = 5/2, M_S\rangle$ spin basis, the Boltzmann factors and spin expectation values can then be obtained. The calculated VTVH curves are fitted to the experimental curves using a least-squares method by varying the spin Hamiltonian parameters. These fitted curves are shown as the solid

(55) A dipole−dipole broadened spectrum was observed for **3** (results not shown).

(56) Neese, F.; Solomon, E. I. *Inorg. Chem.* **1999**, *38*, 1847.

lines in Figure 7 and are obtained using the parameters given in Table 2. The trend is the same as that obtained from the EPR spectra, but the values are significantly smaller. This is not surprising, as the EPR experiments were obtained with powdered solids, while the MCD data were obtained from the samples that were frozen glass solutions where conformational relaxation from the solid state structure is possible.

**(d). Electronic Structure and Hammett Parameters.** The Hammett parameter $\sigma_p$ can qualitatively describe the electronic substituent effect of the structure on the reactivity of a site X in the series $p\text{-}XC_6H_4Y$ for different functional groups Y. This effect is one of many such linear free-energy relationships (LFERs) that have been developed,[57,58] and provides a simple measure of the electron withdrawing ($\sigma_p > 0$) or donating ($\sigma_p < 0$) ability of the functional group relative to Y = H. Values of $\sigma_p$ for complexes **1**−**4** are given in Table 2, and they rank the electron withdrawing ability in the order $-CH_3 < -H < -Br < -NO_2$. One might expect a longer Fe−O bond to the substituted phenolate (Fe−O4) for the $-NO_2$ substituted complex, but in the structural data for these complexes given in Table 1, little experimental variation in Fe−O4 is observed. However, as will be discussed below, although the $Fe^{III}-O_{phenolate}$ bond length is little affected by variation of the substituents, both the $\lambda_{max}$ in the visible spectrum and the half-wave redox potential of the $Fe^{III}/Fe^{II}$ process are strongly influenced by the electron withdrawing or donating nature of the substituents at the *para* position of the terminal $Fe^{III}$-bound phenolate. It is interesting to note that the bond which is the most variable in the series (Table 1) is that to the water (Fe−O3). This is the only monodentate terminal ligand; the other coordinating atoms are constrained by the conformation of the **L-R$^{2-}$** ligand. At least for complexes **1** and **2** it is possible to observe that the $-CH_3$ substituent has an effect on the $Fe^{III}-OH_2$ bond distance since this distance increases to 2.112 Å in $[Fe^{III}Zn^{II}(\mu\text{-}OH)(H_2O)\textbf{L-CH}_3]^{2+}$ when compared with the isostructural complex containing the **L-H$^{2-}$** ligand (2.054 Å).

A graphical representation of the $\alpha$-HOMO and $\beta$-LUMO orbitals for complex **2** is shown in Figure 8. As can be seen, both the $\pi$ orbitals from the terminal phenolate group and the d orbital from the $Fe^{III}$ contribute to this orbital. The d-orbital has mainly $d_{z^2}$ character as expected for a tetragonal compression along the O1−Fe−O4 axis. A linear correlation was obtained (Figure 9a) by plotting the calculated energies of the $\alpha$-HOMO for the complexes **1**−**4** against the Hammett parameter ($\sigma_p$) for the substituents $-CH_3$, $-H$, $-Br$, and $-NO_2$, respectively.

Similarly, as shown in the plot in Figure 9b, the LMCT process is shifted to a lower wavelength (higher energy) as the electron-withdrawing effect of the substituent group increases. Consequently, a hypsochromic shift is observed for $[Fe^{III}Zn^{II}(\mu\text{-}OH)(H_2O)\textbf{L-NO}_2]^{2+}$, whereas the complex $[Fe^{III}Zn^{II}(\mu\text{-}OH)(H_2O)\textbf{L-CH}_3]^{2+}$ shows a bathochromic shift when compared to $[Fe^{III}Zn^{II}(\mu\text{-}OH)-(H_2O)\textbf{L-H}]^{2+}$. The band at 353 nm in the spectrum of $[Fe^{III}Zn^{II}(\mu\text{-}OH)(H_2O)\textbf{L-NO}_2]^{2+}$ is shifted with respect to the other complexes because of an overlap between the LMCT process and $\pi$-phenolate-to-NO$_2$ intraligand
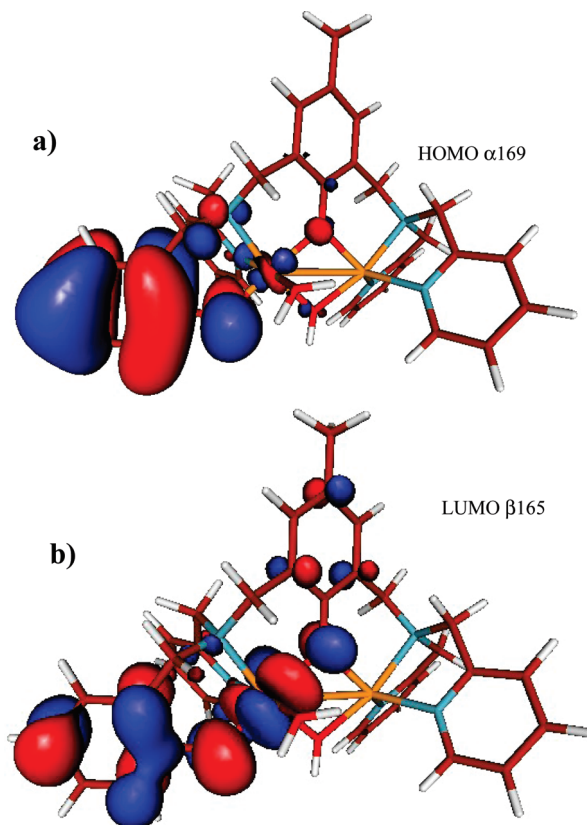


**Figure 8.** Representation of the $\alpha$-HOMO (a) and $\alpha$-LUMO (b) orbitals for complex **2**.

charge transfer transition, which is also observed in the spectrum of the free ligand. This shift was also found previously for a similar nitro substituted phenolate ligand.[21]

**Electrochemical Properties of the Complexes.** The electrochemical behavior of complexes **1**−**4** was studied by cyclic voltammetry (CV) and square wave voltammetry (SW) in an ethanol/water 70/30% v/v solution, and the SW data obtained at pH values of 3.5 and 6.5 are listed in Table 2. For all complexes the cyclic voltammograms show one reversible redox process which can be attributed to the $Fe^{III}/Fe^{II}$ redox couple. Typical square wave voltammograms at distinct pH values for the $[Fe^{III}Zn^{II}(\mu\text{-}OH)(H_2O)\textbf{L-H}]^{2+}$ complex are shown in Figure 10.

When square wave voltammograms for **1**−**4** are recorded at pH 3.5 a process at 60−70 mV versus NHE is observed which becomes cathodically shifted when the pH of the solution is raised to 6.5. We interpret this result as being a consequence of deprotonation of the $Fe^{III}$-bound water molecule (generation of $Fe^{III}-OH$ species) which causes an increase of the electron density on the $Fe^{III}$ center, thus making it more difficult to reduce. On the other hand, one can observe that within the series of complexes **1**−**4**, the half-wave ($E_{1/2}$) potentials become more positive as the electron-withdrawing capacity of the *para* substituent group on the terminal $Fe^{III}$-bound phenolate increases ($-CH_3 < -H < -Br < -NO_2$), a clear indication that the electron spin density around the $Fe^{III}$ center is strongly dependent on the electronic nature of the *para*-substituent (Figure 9c). While the donor effect of the methyl group results in a greater stabilization of the

(57) March, J. *Advanced Organic Chemistry: Reactions, Mechanisms and Structure*, 5th ed.; John Wiley & Sons: New York, 2001.
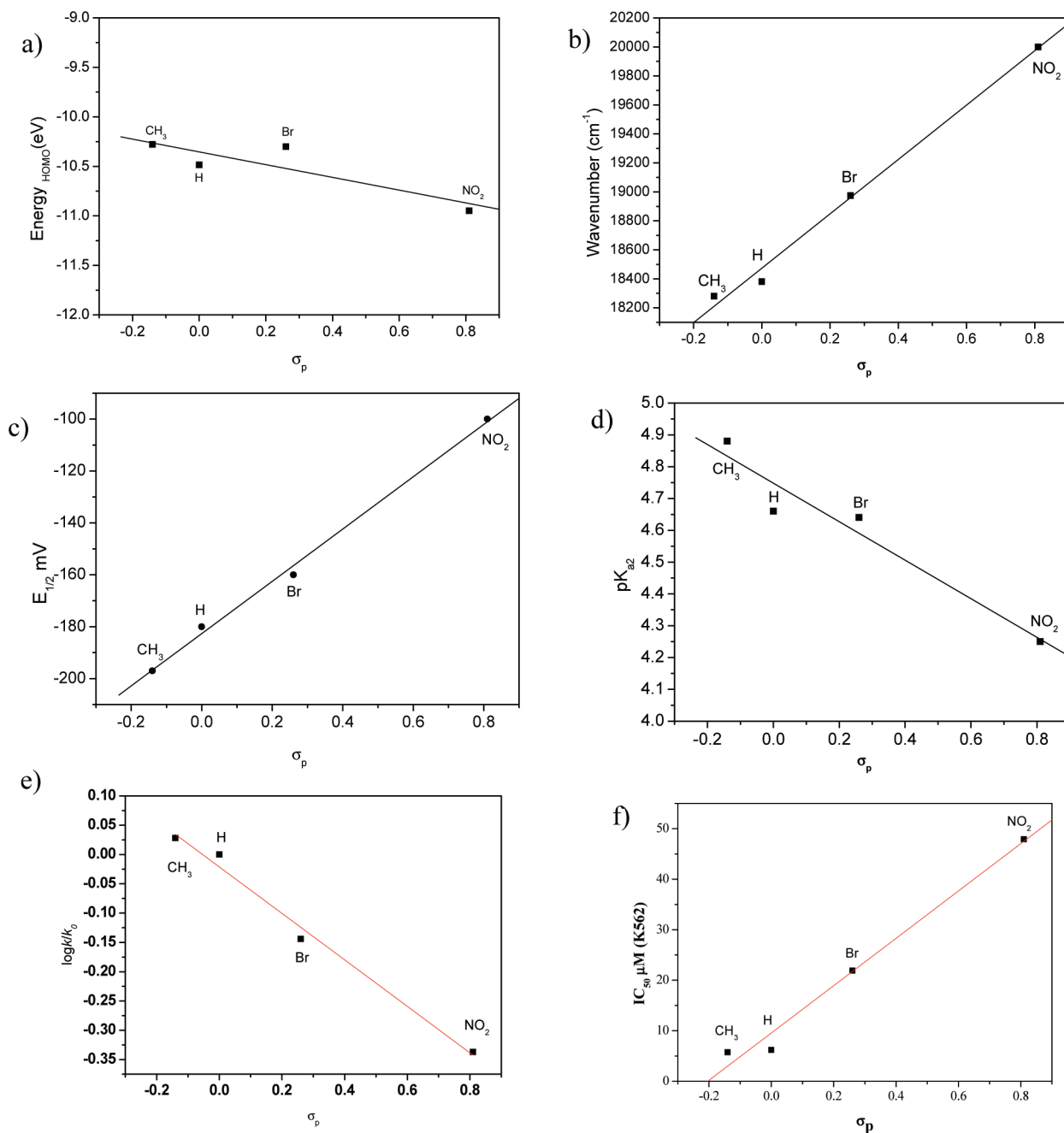(58) Simón-Manso, Y. *J. Phys. Chem. A* **2005**, *109*, 2006.

**Figure 9.** Linear correlation from Hammett parameter ($\sigma_p$) and (a) calculated energies of the $\alpha$-HOMO for the complexes **1−4**; (b) the lowest LMCT band for complexes **1−4**, in CH$_3$CN; (c) the half-wave potentials ($E_{1/2}$) for Fe$^{III}$/Fe$^{II}$ at pH 6.5 for complexes **1−4**. Data obtained from square wave voltammograms (pulse = 20 mV, frequency = 50 Hz) of [Fe$^{III}$Zn$^{II}$($\mu$-OH)(H$_2$O)**L-R**]$^{2+}$ complexes, in ethanol/water 70/30% v/v solution. [complex] = $5.0 \times 10^{-4}$ mol L$^{-1}$, $I$ = 0.1 mol L$^{-1}$ NaCl; carbon working electrode, platinum wire auxiliary electrode, reference: Ag/AgCl (NaCl 3 mol L$^{-1}$); internal standard: K$_3$[Fe(CN)$_6$]); (d) the potentiometric p$K_{a2}$ of complexes **1−4**. (e) Hammett correlation for the hydrolysis of 2,4-bdnpp promoted by complexes **1−4**. (f) Hammett relationship for IC$_{50}$ for K562 and complexes **1−4**. IC$_{50}$ is the concentration required to inhibit 50% of cell growth. The mean IC$_{50}$ ± SD was determined in three independent experiments each performed in duplicate.

3+ oxidation state of the Fe$^{III}$ center, the opposite occurs for [Fe$^{III}$Zn$^{II}$($\mu$-OH)(H$_2$O)**L-NO$_2$**]$^{2+}$, where the 2+ oxidation state of the iron is more stabilized by the electron-withdrawing effect of the nitro group. Interestingly, not only does the $\lambda_{max}$ (500−600 nm; Table 2) of the lowest LMCT band correlate well with the Hammett parameter ($\sigma_p$)[57] but also the half-wave potentials of the Fe$^{III}$/Fe$^{II}$ couple (Figures 9b and 9c). This indicates that the observed effects of the substituent groups on the spectral and redox properties affect the HOMO energies to the same extent (Supporting Information, Figure S3), thus

demonstrating that the theoretical calculations adequately describe the electronic behavior of **1−4**. Indeed, the effects of the substituents on the electronic properties of the biomimetics will be of crucial significance in discussing the factors that determine the differences in the catalytic activities of **1−4** in the hydrolysis of the model diester 2,4-bdnpp and DNA cleavage (vide infra).

**Potentiometric Titrations of the Complexes.** Potentiometric titration studies of **1−4** in a water/ethanol (30:70) solution[6,8,14] showed the neutralization of 3 mol of KOH/mol of complex in the pH range 2−10. The corresponding
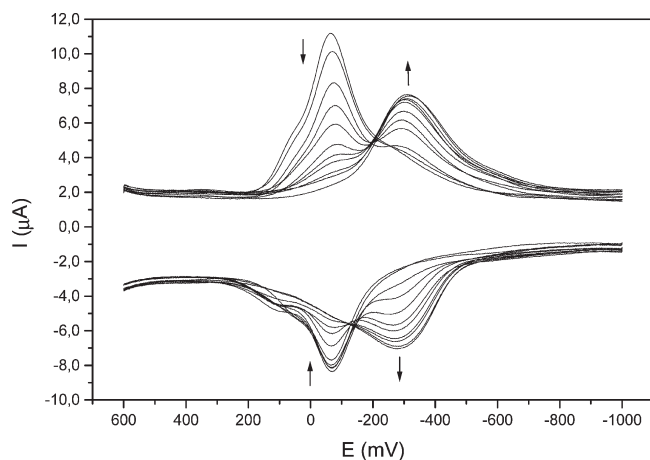
**Figure 10.** Square wave voltammograms (pulse = 20 mV, frequency = 50 Hz) of $[Fe^{III}Zn^{II}(\mu\text{-OH})(H_2O)\mathbf{L\text{-}H}]^{2+}$ by varying pH from 3.5 to 6.50 in pH intervals of 0.25, in ethanol/water 70/30% v/v solution. [complex] = $5.0 \times 10^{-4}$ mol $L^{-1}$, $I$ = 0.1 mol $L^{-1}$ NaCl; carbon working electrode, platinum wire auxiliary electrode, reference: Ag/AgCl (NaCl 3 mol $L^{-1}$); internal standard: $K_3[Fe(CN)_6]$].

**Table 3.** Kinetic and Potentiometric $pK_a$'s for Complexes **1−4**

| complex | kinetic pH optimum | kinetics | | potentiometric | | |
| --- | --- | --- | --- | --- | --- | --- |
| | | $pK_1$ | $pK_2$ | $pK_{a1}$ | $pK_{a2}$ | $pK_{a3}$ |
| **1** | $6.5 \pm 0.5$ | $5.5 \pm 0.1$ | $8.7 \pm 0.2$ | 3.28 | 4.88 | 8.43 |
| **2** | $7.0 \pm 0.5$ | $5.1 \pm 0.2$ | $8.1 \pm 0.2$ | 3.01 | 4.66 | 8.25 |
| **3** | $6.5 \pm 0.5$ | $5.0 \pm 0.2$ | $8.0 \pm 0.2$ | 2.73 | 4.64 | 7.80 |
| **4** | $6.5 \pm 0.5$ | $5.0 \pm 0.2$ | $8.3 \pm 0.1$ | 2.55 | 4.25 | 8.25 |

$pK_a$ values are given in Table 3, and speciation plots are shown in the Supporting Information, Figure S4. For all of the complexes, the first dissociation constant ($pK_{a1}$) can be attributed to the deprotonation of a $\mu$-aqua species in the equilibrium

$$[(OH_2)Fe(\mu\text{-}OH_2)Zn(OH_2)] \text{ (A)}$$
$$\rightleftharpoons [(OH_2)Fe(\mu\text{-}OH)Zn(OH_2)] \text{ (B)} \qquad (6)$$
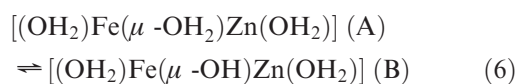
while $pK_{a2}$ and $pK_{a3}$ are attributed to the deprotonation of terminally coordinated water molecules at the $Fe^{III}$ site and the $Zn^{II}$ site, respectively, according to the following equilibria:

$$[(OH_2)Fe(\mu\text{-}OH)Zn(OH)] \text{ (B)}$$
$$\rightleftharpoons [(OH)Fe(\mu\text{-}OH)Zn(OH_2)] \text{ (C)}$$
$$\rightleftharpoons [(OH)Fe(\mu\text{-}OH)Zn(OH)] \text{ (D)} \qquad (7)$$
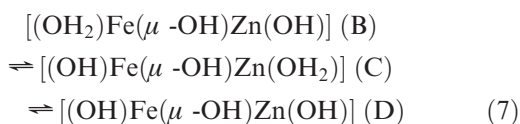
Species B is the same as that determined by X-ray crystallography but with an additional Zn-coordinated water molecule. It is worth noting that the $pK_{a2}$ values attributed to deprotonation of the terminal $Fe^{III}$-bound water for complexes **1−4** also have a linear dependence on the Hammett parameters (Figure 9d). In fact, the dependence of the $pK_a$ values on the Hammett parameters, as well as the linear relationships discussed in the previous section, shows the strong influence of the ligand on the electron spin density on the $Fe^{III}$ center as the electron donor/acceptor nature of the ligand substituent is changed. Thus, as
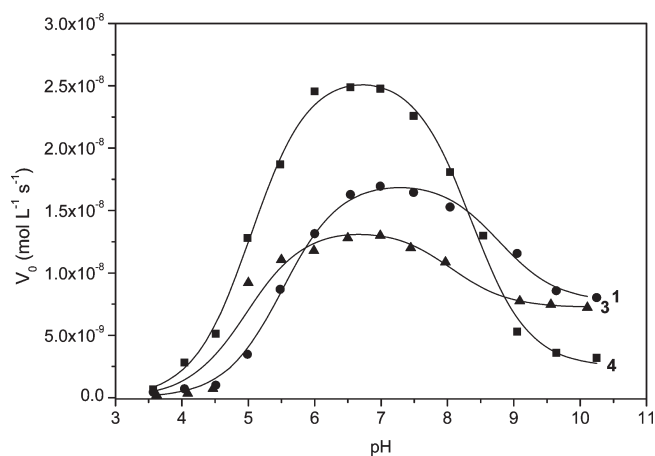


**Figure 11.** Dependence of the initial reaction rate ($V_0$) on pH for the hydrolysis of 2,4-bdnpp promoted by complexes **1**, **3**, and **4**, respectively. [complex] = $4.0 \times 10^{-5}$ mol $L^{-1}$ for complexes **1** and **3** and $6.0 \times 10^{-5}$ mol $L^{-1}$ for complex **4**; [2,4-bdnpp] = $5.0 \times 10^{-3}$ mol $L^{-1}$; [buffers] = 0.05 mol $L^{-1}$; $I$ = 0.05 mol $L^{-1}$ (LiClO$_4$) in $H_2O/CH_3CN$ (1:1) at 25 °C. Data for **2** has been given previously.[14]

expected within the series **1−4**, the $[Fe^{III}Zn^{II}(\mu\text{-OH})(H_2O)\mathbf{L\text{-}CH_3}]^{2+}$ complex shows the highest $pK_{a2}$ value, while the $[Fe^{III}Zn^{II}(\mu\text{-OH})(H_2O)\mathbf{L\text{-}NO_2}]^{2+}$ derivative has the lowest.[59]

**Phosphodiesterase-Like Activity of the Complexes.** It is important to note that complexes **1−4** possess the following features which are required for developing biomimetics of this type: (i) *cis*-oriented labile water molecules to coordinate the substrate and provide a $H_2O/OH^-$ molecule as the nucleophile and (ii) a low $pK_a$ value for one of the water molecules coordinated to the $Fe^{III}$ center, generating a good nucleophile under physiological pH conditions. This last characteristic is present in all four complexes and is strongly influenced by the *para* substituent group on the terminal $Fe^{III}$-bound phenolate as can be observed in the $pK_a$'s obtained (Table 3).

The phosphodiesterase-like activity of complexes **1−4** was evaluated in the hydrolysis reaction of the activated substrate 2,4-bdnpp[26] and monitored spectrophotometrically at 400 nm, and the extinction coefficients of the product 2,4-dinitrophenolate were measured at different pH's under the same experimental conditions of the kinetic measurements: (pH/$\varepsilon$, $M^{-1}$ cm$^{-1}$: 3.5/2125; 4.0/3410; 4.5/7180; 5.0/10080; 5.5/11400; 6.0/12000; 6.5−10.25/12100 for the 2,4-dnp anion) at 25 °C. The pH dependence of the catalytic activity between pH 3.5 and pH 10.25 shows bell-shaped profiles with optima at pH 6.5, 7.0, 6.5, and 6.5 for complexes **1−4**, respectively (Table 3, Figure 11). Overall, these values are in the range found for the $[M^{III}M^{II}(\mu\text{-OAc})_2(\mathbf{L\text{-}H})]$ complexes[6,9,11,14] under similar experimental conditions and for PAPs.[2] For each complex, the reaction is strongly influenced by the pH and the bell-shaped pH dependence of the reactivity indicates that at least two protonation equilibria ($pK_1 = pK_{a2}$ and $pK_2 = pK_{a3}$) are relevant to catalysis (Table 3), in good agreement with the values of the $pK_a$'s obtained from potentiometric titration. Indeed these data suggest that deprotonation of the $Fe^{III}$-coordinated water

(59) Potentiometric Titration of complexes **1−4** in water/CH$_3$CN (50:50) results in a similar trend of the $pK_a$ values obtained in water/ethanol (30/70) with $pK_a$'s in water/CH$_3$CN being ∼0.15 pH units higher.

**Table 4.** Kinetic Parameters for the Hydrolysis of 2,4-bdnpp, Catalyzed by Complexes **1–4**[a]

| complex | $V_{max}$ (mol L$^{-1}$ s$^{-1}$) | $K_M$ (mol L$^{-1}$) | $k_{cat}$ (s$^{-1}$) | $k_{cat}/K_M$ (mol$^{-1}$ L s$^{-1}$) | $K_{assoc}$ (mol$^{-1}$ L) | $k_{cat}/k_{nc}$ |
|---|---|---|---|---|---|---|
| **1** | $3.68 \pm 0.15 \times 10^{-8}$ | $3.05 \pm 0.10 \times 10^{-3}$ | $9.20 \times 10^{-4}$ | $30 \times 10^{-2}$ | 327 | $4.9 \times 10^{3}$ |
| **2** | $3.50 \pm 0.12 \times 10^{-8}$ | $4.20 \pm 0.09 \times 10^{-3}$ | $9.13 \times 10^{-4}$ | $20 \times 10^{-2}$ | 238 | $4.8 \times 10^{3}$ |
| **3** | $2.64 \pm 0.09 \times 10^{-8}$ | $6.97 \pm 0.11 \times 10^{-3}$ | $6.55 \times 10^{-4}$ | $9.5 \times 10^{-2}$ | 143 | $3.5 \times 10^{3}$ |
| **4** | $1.85 + 0.10 \times 10^{-8}$ | $2.58 \pm 0.07 \times 10^{-3}$ | $4.63 \times 10^{-4}$ | $18 \times 10^{-2}$ | 387 | $2.5 \times 10^{3}$ |

[a] Conditions: CH$_3$CN/H$_2$O 1:1; [complex] = $4.0 \times 10^{-5}$ mol L$^{-1}$; [buffer] = 0.05 mol L$^{-1}$ (MES or HEPES); $I$ = 0.05 mol L$^{-1}$ (LiClO$_4$); [2,4-bdnpp] = $1.0$–$8.0 \times 10^{-3}$ mol L$^{-1}$ at 25 °C.

molecule generates the catalytic active species [(OH)Fe$^{III}$-($\mu$-OH)Zn$^{II}$(H$_2$O)] within the series of complexes **1–4**, although it does not necessarily discriminate whether the initiating nucleophile is the terminal or the bridging Fe$^{III}$-bound hydroxo group. The dependence of the initial rates, at optimal pH for **1–4**, on the concentration of the substrate reveals saturation kinetics with Michaelis–Menten-like behavior. The resulting $k_{cat}$ and $K_M$ parameters were obtained by fitting the data ($V_0$ vs [bdnpp], Supporting Information, Figure S5) using the non-linear regression of the Michaelis–Menten equation, and the values are listed in Table 4.

For the complexes **1–4**, increasing catalytic activity is measured (Table 4) in the following sequence of ligands: **L-CH$_3$ (1)** > **L-H (2)** > **L-Br (3)** > **L-NO$_2$ (4)**. The complexes **1–2** and **3–4** show, respectively, ~100 and 10 turnovers in 24 h at pH = 6.5 and 25 °C. To evaluate the monoesterase activity of **1–4**, 1:1 stoichiometric reactions between the complexes and the phosphate diester 2,4-bdnpp were carried out. As observed previously,[14,41] after 55 h at 50 °C one 2,4-bdnp molecule is released, indicating that only the diester can be hydrolyzed.

Isotope effect studies for the hydrolytic cleavage of 2,4-bdnpp by **1–4** were carried out under identical conditions using H$_2$O or D$_2$O to probe the possibility of a general base reaction mechanism. If the solvent deuterium isotope effect $k_H/k_D$ of identical reactions remains between 0.80 and 1.50, no proton transfer is present in the rate-limiting step of the reaction.[60] Complexes **1–4** show $k_H/k_D$ values of 1.03, 1.34,[14] 1.12, and 0.93, respectively, providing further evidence for an intramolecular nucleophilic attack in the hydrolysis of 2,4-bdnpp promoted by these complexes.

As discussed in the previous sections, the *para* substituents on the terminal Fe$^{III}$-bound phenolate strongly influence the electronic properties of the Fe$^{III}$ center demonstrated through several linear relationships involving the dependence of these electronic properties (Figure 9) on the Hammett parameters. Particularly interesting is the fact that the p$K_{a2}$ values attributed to deprotonation of the terminally Fe$^{III}$-bound water for complexes **1–4** have a linear dependence on the Hammett constants, providing evidence that the Lewis acidity of the Fe$^{III}$ center is directly affected as the electron donor/acceptor nature of the ligand substituent is changed.

The hydrolysis reactions of the phosphate diester 2,4-bdnpp catalyzed by the series of complexes **1–4** under identical experimental conditions reveal that the turnover rate ($k_{cat}$) decreases in the following sequence of substituents: $-CH_3$ > $-H$ > $-Br$ > $-NO_2$. While complex **1** containing the $-CH_3$ substituent and the highest p$K_{a2}$ shows the highest catalytic reactivity, the [Fe$^{III}$Zn$^{II}$($\mu$-OH)(H$_2$O)-**L-NO$_2$**]$^{2+}$ derivative has the lowest p$K_{a2}$ and the lowest

**Scheme 1.** Mechanism Proposed for the Hydrolysis of 2,4-bdnpp by Complexes **1–4**
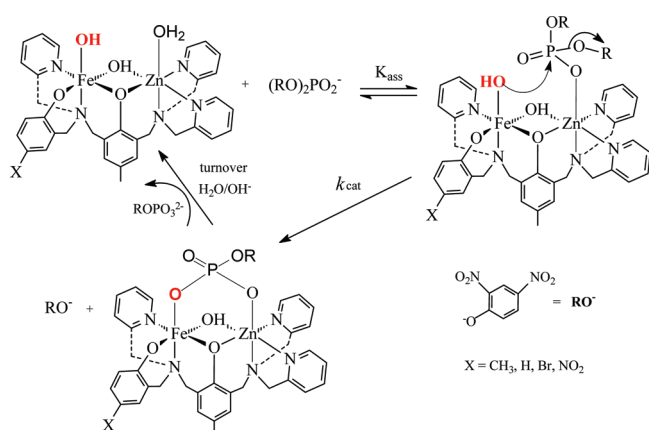


turnover number (Table 4). It is important to emphasize that within the series of complexes investigated, the structural unit [(OH)Fe$^{III}$($\mu$-OH)Zn$^{II}$(OH$_2$)] of the catalyst is maintained in solution as demonstrated by the potentiometric titration experiments (vide supra) and thus the observation of different p$K_{a2}$'s (nucleophiles) and turnover rates must be intrinsically related to the change of the donor/acceptor nature of the *para*-substituent on the terminal Fe$^{III}$-bound phenolate.

Interestingly, a $\rho$ value of $-0.60$ for the Hammett plot on p$K_{a2}$ (Figure 9d) arises from the strength of the interaction between the aryl substituents and the acidic water bound to the Fe$^{III}$ center. This interaction depends on the distance between the interacting sites and the identity of the intervening groups. In the simplest case, substituted phenols have no intervening groups and exhibit a $\rho$ = $-2.23$ for p$K_a^{PhOH}$.[61] In contrast, the polar substituent effect on the p$K_{a2}$ of the acidic water in **1–4** is transmitted through the aryl oxygen atom and the ligand-bound Fe$^{III}$ causing a lower dependence on the $\rho$ value. This dependence relates to the product of "attenuation factors" ($f$) for each intervening group in the phenol, that is, $\rho = \rho_{phenol} f_O f_{Fe}$. Using $f_O$ = 0.64 from the literature,[61] a value of 0.42 is calculated for $f_{Fe}$.[61]

In addition, a LFER is found when $\log(k_{cat}/k_0)$ is plotted against the Hammett parameter $\sigma$ (Figure 9e), and a least-squares treatment of the data gives a $\rho$ value of $-0.40$. Indeed, the $\rho$ value of $-0.40$ for the Hammett plot on $k_{cat}$ is also a function of the distance between the aryl substituents and the nucleophilic hydroxide, but lies 0.2 units above the $\rho$ value for p$K_{a2}$, which in relation to a single proton is a consequence of the lower affinity of the phosphoryl group by the metal coordinated hydroxo. The

(60) Deal, K. A.; Hengge, A. C.; Burstyn, J. N. *J. Am. Chem. Soc.* **1996**, *118*, 1713–1718.

(61) Williams, A. *Free Energy Relationships in Organic and Bio-organic Chemistry*; Royal Society of Chemistry: Cambridge, 2003.
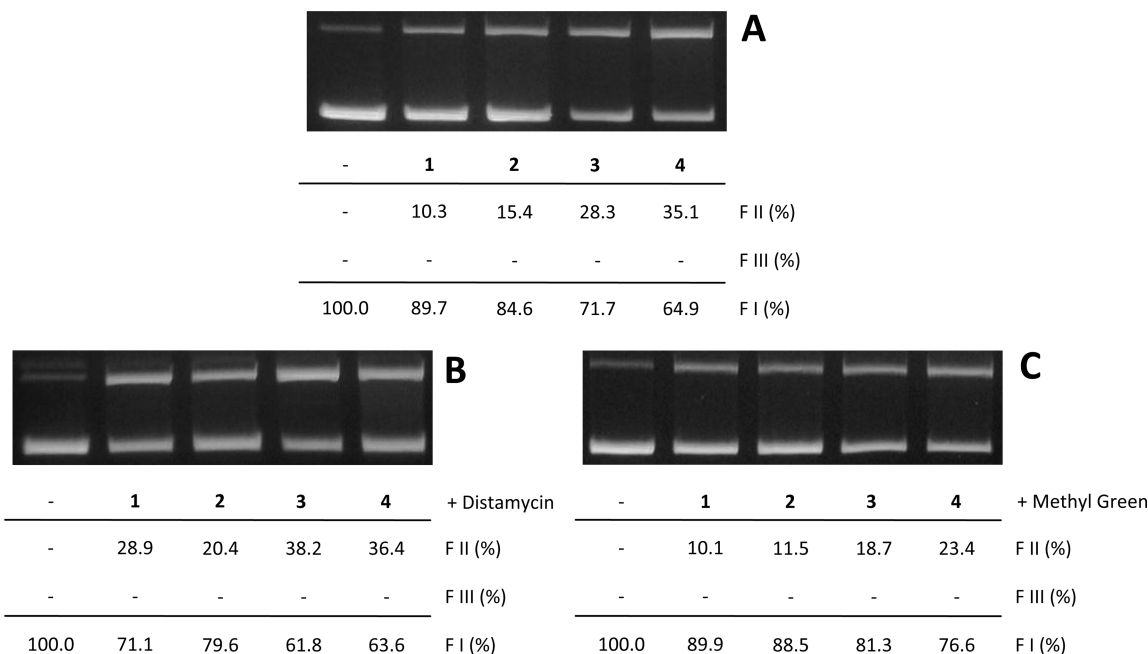
| - | 1 | 2 | 3 | 4 | |
|---|---|---|---|---|---|
| - | 10.3 | 15.4 | 28.3 | 35.1 | F II (%) |
| - | - | - | - | - | F III (%) |
| 100.0 | 89.7 | 84.6 | 71.7 | 64.9 | F I (%) |

| - | 1 | 2 | 3 | 4 | + Distamycin |
|---|---|---|---|---|---|
| - | 28.9 | 20.4 | 38.2 | 36.4 | F II (%) |
| - | - | - | - | - | F III (%) |
| 100.0 | 71.1 | 79.6 | 61.8 | 63.6 | F I (%) |

| - | 1 | 2 | 3 | 4 | + Methyl Green |
|---|---|---|---|---|---|
| - | 10.1 | 11.5 | 18.7 | 23.4 | F II (%) |
| - | - | - | - | - | F III (%) |
| 100.0 | 89.9 | 88.5 | 81.3 | 76.6 | F I (%) |

**Figure 12.** Supercoiled DNA cleavage by **1**−**4** (30 $\mu$mol L$^{-1}$) in PIPES buffer (pH 6.5, 25 mmol L$^{-1}$) in the absence (A) and in the presence of Distamycin (50 $\mu$mol L$^{-1}$) (B) and in the presence of Methyl green (50 $\mu$mol L$^{-1}$) (C) for 16 h at 50 °C.

Brønsted plot of log $k_{cat}$ versus the p$K_{a2}$ of the Fe$^{III}$−OH$_2$ (Supporting Information, Figure S6) exhibits a good linear correlation with a $\beta_{nuc}$ = 0.60. This value is substantially higher than those observed for the uncatalyzed hydrolyses of phosphate diesters and triesters ($\beta_{nuc}$ values around 0.30),[62,63] therefore indicating that the hydroxide-catalyzed hydrolysis of the 2,4-bdnpp involves a more nucleophilic contribution in the transition state.

In summary, given that complexes **1**−**4** are structurally very similar and that the difference in reactivity results from varying the strength of the nucleophile (Fe−OH) because of the change of the *para*-substituent on the terminal Fe-bound phenolate, as evidenced from the LFER/Hammett plot (Figure 9e), a common reaction coordinate/transition state and thus a common mechanism, as shown in Scheme 1, is proposed for the hydrolysis reaction of the phosphate diester 2,4-bdnpp by these complexes.[14] In the first phase of the mechanism [(OH)Fe$^{III}$($\mu$-OH)Zn$^{II}$(OH$_2$)] is the catalytically active species and possesses a labile site that permits the monodentate binding of the substrate to the Zn$^{II}$ center. This hypothesis is strongly supported by EPR spectroscopic data of **2**, measured in the absence and presence of 2,4-bdnpp, which indicate that the substrate does not interact with the Fe$^{III}$ center.[14] Next, an intramolecular nucleophilic attack by the *cis* oriented Fe$^{III}$-bound hydroxide leads to the release of 2,4-dinitrophenolate with the monoester 2,4-dinitrophenyl-phosphate remaining coordinated to the complex; and finally, the $\mu$-1,3-coordinated monoester intermediate undergoes substitution by two water molecules and regenerates the active site for the next catalytic cycle. This proposal, as shown in Scheme 1, is in accordance with the X-ray structure of a tetranuclear Fe$_2$Zn$_2$ complex bridged by inorganic phosphate that has been determined as the end product resulting from the dimerization of catalyst **2** in a significantly slower reaction.[14] Therefore, it has been concluded that the

$\mu$-hydroxo is a significantly poorer nucleophile than the terminally Fe$^{III}$-bound hydroxo group, and that hydrolysis of the monoester to form inorganic phosphate and 2,4-dinitrophenolate occurs exclusively because of the background reaction.

**DNA Cleavage Catalyzed by 1−4.** Data on DNA cleavage by the complexes **1**−**4** indicated that all complexes are able to moderately cleave the plasmid DNA after 16 h at 50 °C and low concentration (30 $\mu$mol L$^{-1}$), converting the plasmid supercoiled DNA into open circular DNA (Figure 12A). All of ROS scavengers did not inhibit the DNA cleavage performed by **1**−**4** clearly suggesting that the DNA scission mechanism maybe follows a hydrolytic rather than oxidative pathway (Supporting Information, Figure S7). Then, the proposed mechanism of 2,4-bdnpp hydrolysis can be also illustrate to the DNA cleavage event.

Distamycin did not prevent the DNA cleavage by **1**−**4**, but on the contrary enhanced the DNA fragmentation (Figure 12B). This effect may be attributed to the distamycin binding at the DNA minor groove, modifying the DNA structure in such a way that it enhances the binding affinity of the complexes, as observed for other examples in the literature.[65] On the other hand, methyl green did not affect the DNA cleavage promoted by **1** and **2**, but slightly decreases the activity of **3** and **4**. Regarding these results it is difficult to suggest an appropriate mechanism of complex-DNA interaction. However, a DNA-groove binding mode cannot be ruled out by these assays.

The DNA cleavage kinetic behavior was investigated with concentration dependence on complexes **1**−**4**. When the obtained DNA cleavage rates ($k_{obs}$) were plotted

(62) Khan, S. A.; Kirby, A. J. *J. Chem. Soc.* **1970**, 1172–1182.
(63) Kirby, A. J.; Younas, M. *J. Chem. Soc.* **1970**, 1165–1172.

(64) Sreedhara, A.; Freed, J. D.; Cowan, J. A. *J. Am. Chem. Soc.* **2000**, *122*, 8814–8824.
(65) Ferrer, S.; Ballesteros, R.; Sambartolome, A.; Gonzalez, M.; Alzuet, G.; Borras, J.; Liu, M. *J. Inorg. Biochem.* **2004**, *98*, 1436–1446. Thomas, A. M.; Nethaji, M.; Mahadevan, S.; Chakravarty, A. R. *J. Inorg. Biochem.* **2003**, *94*, 171–178.
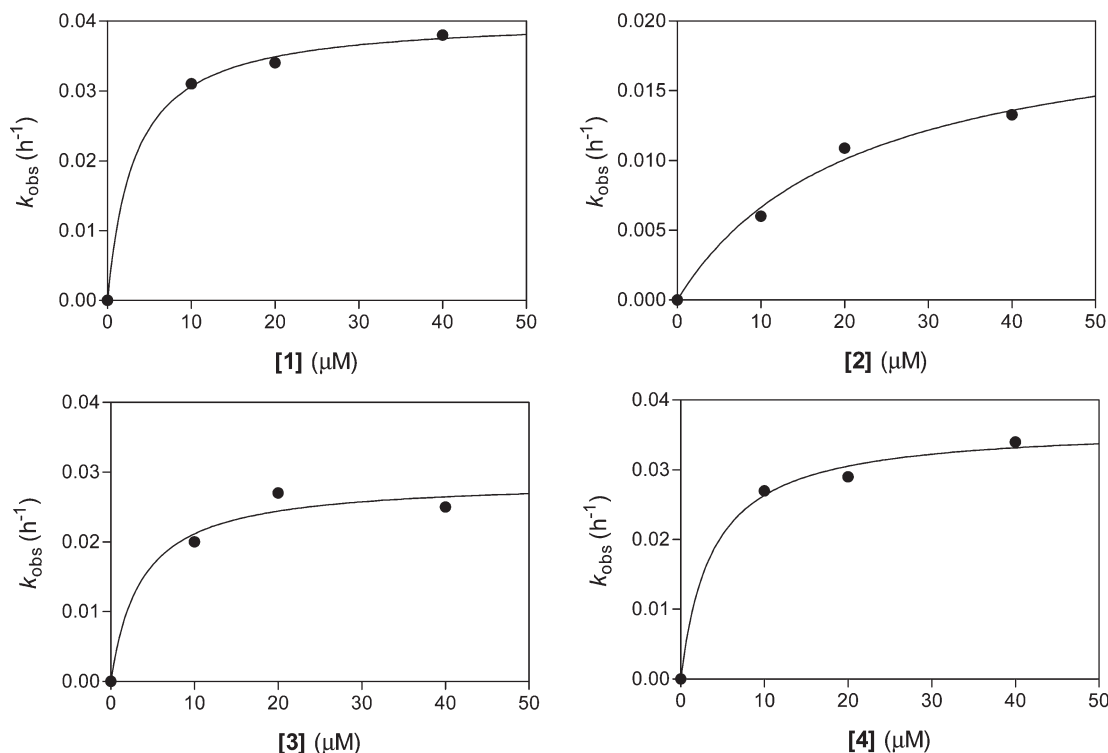
**Figure 13.** Kinetics of supercoiled DNA cleavage by **1**−**4** at pH 6.5 under *pseudo*-Michaelis−Menten conditions. Conditions: [plasmid DNA] = 30 $\mu$mol L$^{-1}$; [complex] = 0−40 $\mu$mol L$^{-1}$; [PIPES buffer] = 25 mmol L$^{-1}$ at 50 °C. Samples were collected at 0, 60, 120, 240, 360, and 480 min.

**Table 5.** Kinetic DNA Degradation Parameters Obtained for the Complexes **1**−**4**

| kinetic parameters | 1 | 2 | 3 | 4 |
|---|---|---|---|---|
| $k_{cat}$ (h$^{-1}$) | $4.05 \times 10^{-2}$ | $2.09 \times 10^{-2}$ | $2.89 \times 10^{-2}$ | $3.63 \times 10^{-2}$ |
| $K_M$ (mol L$^{-1}$) | $3.23 \times 10^{-6}$ | $21.4 \times 10^{-6}$ | $3.66 \times 10^{-6}$ | $3.73 \times 10^{-6}$ |
| $k_{cat}/K_M$ (mol$^{-1}$ L h$^{-1}$) | $1.39 \times 10^{4}$ | $0.98 \times 10^{4}$ | $0.79 \times 10^{4}$ | $0.97 \times 10^{4}$ |
| $E$ ($k_{cat}/k_{unc}{}^{a}$) | $11.2 \times 10^{5}$ | $5.8 \times 10^{5}$ | $8.0 \times 10^{5}$ | $10.0 \times 10^{5}$ |

$^{a}$ Spontaneous dsDNA hydrolysis ($3.6 \times 10^{-8}$ h$^{-1}$)[64]

**Table 6.** IC$_{50}$ Values for Complexes **1**, **2**, **3**, and **4**

| | IC$_{50}$ ($\mu$M ± s.d.) | |
|---|---|---|
| complex | GLC4 | K562 |
| 1 | 6.3 ± 0.6 | 5.73 ± 0.6 |
| 2 | 4.37 ± 0.4 | 6.2 ± 0.5 |
| 3 | | 21.9 ± 2.0 |
| 4 | 18.2 ± 1.9 | 47.9 ± 4.0 |

against the complexes' concentration, the $k_{obs}$ values reach a saturation behavior, proper of a pseudo-Michaelis−Menten behavior (Figure 13). The kinetic parameters obtained under these experimental conditions from these plots are summarized in Table 5. Indeed, these results also support the hydrolytic mechanism of DNA cleavage, since metal complexes with oxidative DNA scission mechanism usually do not follow a saturation behavior. On the basis of $k_{cat}$ values, the activity order of DNA cleavage (**1** ≅ **4** > **3** > **2**) does not follows the trend in reactivity observed in the hydrolysis of the 2,4-bdnpp substrate (**1** > **2** > **3** > **4**), which demonstrates that other factors may contribute to complex-DNA interaction rather than the presence of donating and electron withdrawing substituents. Nevertheless, it should be noted that the $K_M$ values for the complexes containing the bulky para-substituents (R = **1**, **3**, **4**) are about 6 times lower in relation to complex **1** (R = H) and thus suggest a higher hydrophobic interaction between the substituted aromatic rings and the hydrophobic groups from other molecules such as the base pairs of DNA.

**Cytotoxicity Activities of the Complexes.** The in vitro cytotoxic activities of complexes **1**−**4** were evaluated against K562 and GLC4 tumor cell lines. The concentrations of

complexes necessary to inhibit 50% of cell growth, IC$_{50}$, are shown in Table 6. By comparing the activity of the complexes, one observes that the effectiveness increases in the order **4** < **3** < **2** < **1**. The efficacy follows the trend of increasing basicity of the active site. As demonstrated above, an electron-withdrawing group such as −NO$_2$ or −Br decreases the basicity of the Fe$^{III}$-bound OH$^-$ group while a hydrogen or a methyl group, by an inductive effect, increases the basicity of the hydroxo group, which acts as the initiating nucleophile in the hydrolysis of phosphate diester bonds (Scheme 1). Interestingly, a linear correlation was found between the Hammett parameter $\sigma_p$ and the IC$_{50}$ values for complexes **1**−**4** (Figure 9f). Nevertheless, on the basis of the experimental results presented in this study, at present we were unable to establish a clear relationship between DNA in vitro cleavage and tumor cell death.

**Conclusion**

Considerable success has been achieved in the synthesis of model complexes that mimic structural and spectroscopic aspects of corresponding enzymatic systems. However, in comparison to their biological counterparts the synthetic systems generally have catalytic efficiencies that are orders of magnitude lower. In the active sites of enzymes, substrates generally bind in a specific orientation relative to some

functional groups within the catalyst, and hydrogen bonds play an important role in binding and orienting substrates optimally. To a large extent the low catalytic efficiency in model systems is associated with their inability to bind and orient substrates in an optimal manner. In the present work we have synthesized and studied the structural and spectroscopic properties of a series of phenolate coordinated iron(III) complexes that resemble the catalytic center of PAPs. Considering that the $Fe^{III}$ plays an essential role in the reaction mechanism of PAPs activating the hydrolysis-initiating nucleophile,[2] the interaction between the phenolate ligand and the metal ion may play an important role in the modulation of the activity. To probe the role of the $Fe^{III}-O_{phenolate}$ bond in the model systems (and, by analogy, the $Fe^{III}$-tyrosinate moiety in PAPs) electron donating and electron withdrawing substituents have been incorporated. The effects of the substituents manifest themselves in a systematic alteration of the electronic properties, mapped through the relationships between the Hammett parameter and various ground and excited state parameters. The electron donating substituents increase, and electron withdrawing substituents decrease the hydrolytic activity of the biomimetic complex toward a model phosphate substrate. The reverse, however (with exception of $[Fe^{III}Zn^{II}(\mu\text{-}OH)(H_2O)\mathbf{L\text{-}NO_2}]^{2+}$), is true for the effect on nuclease activity indicating that the mechanism of hydrolysis for these two activities (i.e., phosphorolysis and nucleolysis) is likely different. These observations suggest that the goal of producing effective biomimetics will be attained through a combination of structural and electronic enhancements in the second coordination sphere which will effectively mimic the substrate binding pockets and relevant hydrogen bonding interactions in naturally occurring systems.[66] The electronic effect of the substituents seems also to impact the ability of complexes to inhibit the growth of tumor cell lines. The cytotoxic activity increases with the electron donating ability which raises the basicity of the hydroxo group acting as a nucleophile. Further studies aiming to establish a clear relationship between DNA in vitro cleavage and tumor cell death by complexes **1**−**4** are underway and will the subject of future reports.

**Supporting Information Available:** Table S1 and Figures S1−S7 in PDF format and crystallographic data in CIF format. This material is available free of charge via the Internet at http://pubs. acs.org. Also, crystallographic data (without structure factors) for the structure(s) reported in this paper have been deposited with the Cambridge Crystallographic Data Centre as supplementary publication nos. CCDC-737630 and CCDC-737631. Copies of the data can be obtained free of charge from the CCDC (12 Union Road, Cambridge CB2 1EZ, U.K.; phone: (+44) 1223−336−408; fax: (+44) 1223−336−003; e-mail: deposit@ccdc.cam.ac.uk; Web site www.ccdc.cam.ac.uk).

(66) Piovezan, C.; Jovito, R.; Bortoluzzi, A. J.; Terenzi, H.; Fischer, F. L.; Severino, P. C.; Pich, C. T.; Azzolini, G. G.; Peralta, R. A.; Rossi, L. M.; Neves, A. *Inorg. Chem.* **2010**, *49*, 2580–2582.